Mechanics of Materials 165 (2022) 104159

Contents lists available at ScienceDirect

Mechanics of Materials

journal homepage: www.elsevier.com/locate/mecmat

Research paper

Nonlinear elastic analysis of 2D materials of arbitrary symmetries with application to black phosphorus

Serge R. Maalouf[1], Senthil S. Vel[*,2]

Department of Mechanical Engineering, University of Maine, Orono, ME 04469, USA

ARTICLE INFO

Keywords:
Nonlinear elasticity
Polynomial constitutive model
Elastic constants
Arbitrary material symmetry
Density functional theory
Black phosphorus

ABSTRACT

Murnaghan's polynomial based nonlinear elastic constitutive model has been previously applied to 2D materials of hexagonal symmetry. We present a general approach for determining the nonlinear elastic constants of 2D materials of arbitrary symmetries and any constitutive polynomial order. The methodology, which is based on ray sampling of the strain energy density in strain space, is independent of the energy calculation method. The ray based methodology is verified by evaluating the elastic constants of graphene which is a hexagonally symmetric 2D material previously considered in the literature. The methodology is then applied to determine the elastic constants of black phosphorus, an orthorhombic 2D material whose comprehensive nonlinear elastic behavior has not been previously considered in the literature. The energy calculations are carried out using plane-wave density functional theory. Detailed convergence analyses are performed to assess the accuracy of the nonlinear elastic constants. The linearized mechanical properties of black phosphorus are obtained from the elastic constants for comparison with the results published in the literature.

1. Introduction

A two-dimensional (2D) material is defined as a material whose atomic structure is composed of one layer of atoms, or a few layers of tightly bonded atomic planes. This class of materials is proving to be increasingly important in different applications (Du et al., 2015; Akinwande et al., 2017; Lee et al., 2013; Fisher, 2018; Xiao et al., 2016; Ling et al., 2015; Inamuddin et al., 2019). Two-dimensional materials span different crystal symmetries from hexagonal (e.g., graphene) to triclinic (e.g., rhenium disulfide). It is necessary to understand the nonlinear elastic behavior of 2D materials of arbitrary symmetries in order to effectively employ them in applications. Black phosphorus, is an example of an orthorhombic 2D material. The mechanical behavior of black phosphorus has been investigated in some papers (Jiang and Park, 2014; Wang et al., 2015; Cao et al., 2017; Li and Yang, 2018; Tao et al., 2015; Setoodeh and Farahmand, 2018; Chen et al., 2016) but a comprehensive framework for the nonlinear elastic behavior of black phosphorus is still lacking which is also the case for many 2D materials of low crystal symmetry.

Several different approaches have been presented in the literature to model the mechanical behavior of certain 2D materials (Xu et al., 2012; Jia, 2015; Fish et al., 2007; Mukhopadhyay et al., 2017; Yang et al., 2016; Davydov, 2011; Cadelano et al., 2009; Ghaffari et al., 2019). A thermodynamically rigorous nonlinear elastic constitutive model, valid for any material symmetry, was proposed by Murnaghan (1937). This model is based on a partial Maclaurin series expansion of the hyperelastic strain energy density in terms of the components of the Green–St. Venant strain tensor. Birch (1947) applied the theory for cubic crystals. Murnaghan's constitutive relation has been successfully used to model a multitude of materials including 2D materials of hexagonal symmetry, e.g., graphene (Wei et al., 2009), silicon carbide (Peng, 2020), germanium carbide (Peng et al., 2013), hexagonal boron-nitride (Peng et al., 2012b), MoS_2 (Cooper et al., 2013), borophene (Faghihnasiri et al., 2019), graphyne (Peng et al., 2012a) and FeB_2 (Ahmadi et al., 2019). In order to model a material using Murnaghan's constitutive relation, it is necessary to determine a set of material specific elastic constants. A larger number of linearly independent elastic constants need to be determined for materials of lower symmetry, e.g., an orthorhombic material has more linearly independent elastic constants than a hexagonal material. Furthermore, a larger number of elastic constants need to be determined as the order of the constitutive polynomial increases.

It is important to develop a systematic methodology to determine the elastic constants of a 2D material that is independent of the material's symmetry and the order of the constitutive polynomial. The

---

* Corresponding author.
E-mail addresses: serge.maalouf@maine.edu (S.R. Maalouf), senthil.vel@maine.edu (S.S. Vel).

[1] Ph.D Student in Mechanical Engineering.

[2] Professor of Mechanical Engineering.

https://doi.org/10.1016/j.mechmat.2021.104159
Received 13 August 2021; Received in revised form 6 November 2021; Accepted 16 November 2021
Available online 6 December 2021

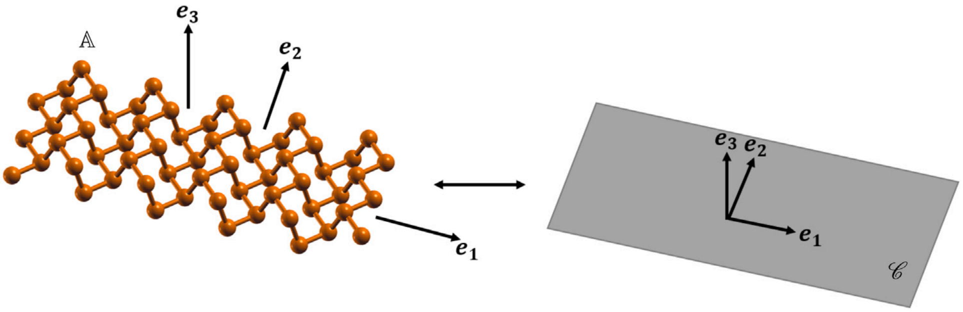

Fig. 1. Equivalent continuum of an arbitrary crystal.

methodology presented in the literature for calculating the elastic constants of 2D materials, primarily of hexagonal symmetry, is based on curve fitting for the elastic constants using the stress–strain curves. In the case of 2D materials of arbitrary symmetries, it is not always clear

(a) how many stress–strain simulations need to be performed,
(b) what deformations need to be applied to the material in each simulation,
(c) in what order the curve fitting should be carried out, especially for increasing constitutive polynomial orders, and
(d) the order of the polynomial necessary to achieve a certain accuracy.

The objective of the current work is to present a systematic methodology to determine the nonlinear elastic constants of 2D materials of arbitrary symmetries. We use Murnaghan's thermodynamically rigorous constitutive model which is based on a polynomial expansion of the strain energy density in terms of the components of the Green–St. Venant strain tensor. While Murnaghan's constitutive model has been previously employed to analyze 2D materials (Wei et al., 2009; Peng, 2020; Peng et al., 2013, 2012b; Cooper et al., 2013; Faghihnasiri et al., 2019; Peng et al., 2012a; Ahmadi et al., 2019), those approaches are tailored towards the analysis of hexagonal materials using up to fifth order polynomial expansions. The present methodology can be used for materials of arbitrary symmetries. Furthermore, in the current methodology, the order of the constitutive polynomial can be increased as needed to accurately capture the nonlinear elastic response of highly strained 2D materials. The methodology is based on ray sampling of the strain energy density in strain space and is independent of the way the strain energy is calculated. The number and direction of the rays, in addition to the number of strain states per ray, can be varied to achieve any desired accuracy in the elastic constants. In the present work, density functional theory is used to calculate the energies. The methodology is verified by comparing the calculated elastic constants of graphene to previously published work. Subsequently, the ray based methodology is used to determine the nonlinear elastic constants of black phosphorus which is an element of the class of materials of orthorhombic symmetry. The comprehensive nonlinear elastic behavior of the latter materials symmetry class has not been previously considered in the literature. Detailed convergence analyses have been performed to assess the accuracy of the elastic constants of black phosphorus. Furthermore, the effect of the order of the constitutive polynomial on the accuracy of the predicted strain energy densities is evaluated.

2. Constitutive model

In the present work, the Einstein summation convention (e.g., see Slaughter (2002)) is used except where otherwise specified and the Voigt and tensorial notations are used interchangeably. Furthermore, $\boldsymbol{E}$, $\boldsymbol{S}$ and W represent the Green–St. Venant strain tensor, the second Piola–Kirchhoff stress tensor and the strain energy density, respectively.

Fig. 1 shows an arbitrary 2D material represented by the crystal $\mathbb{A}$ and its equivalent continuum represented by the domain $\mathscr{C}$. In Fig. 1, and in the rest of this paper, $\boldsymbol{e_1}$ is defined as the longitudinal direction and $\boldsymbol{e_2}$ is defined as the lateral direction. The equivalent continuum, for a material studied at the nanoscale, is defined as a fictitious continuum material having the same dimensions and the same symmetry as the studied crystal in addition to behaving similarly under the same physical conditions. In essence, the equivalent continuum is a hypothetical material that is physically equivalent to the crystal. For example, the strain energy is the same for the same strain state shown in Fig. 1, i.e., $W_{\mathscr{C}} = W_{\mathbb{A}}$. Since the strain energies are the same for any given strain state, the stresses will follow via the hyperelastic constitutive relations (e.g., see Slaughter (2002)) and thus a constitutive model representing the equivalent continuum's behavior represents the crystal's behavior.

Murnaghan (1937) proposed a thermodynamically consistent, nonlinear elastic constitutive model in which they expanded the strain energy density as a partial Maclaurin series in terms of the components of the Green–St. Venant strain tensor. In the present work we use a form similar to the one presented by Hiki (1981), where the total energy density U is expanded in terms of the components of the Green–St. Venant strain tensor $\boldsymbol{E}$ as

$$U = U_0 + C_i E_i + \frac{1}{2!} C_{ij} E_i E_j + \frac{1}{3!} C_{ijk} E_i E_j E_k + \frac{1}{4!} C_{ijkl} E_i E_j E_k E_l + \frac{1}{5!} C_{ijklm} E_i E_j E_k E_l E_m + \dots, \tag{1}$$

where, U_0 is the energy density of the undeformed state, i.e., when $\boldsymbol{E} = \boldsymbol{0}$, and

$$E_1 = E_{11},\ E_2 = E_{22},\ E_3 = E_{33},\ E_4 = 2E_{23},\ E_5 = 2E_{13},\ E_6 = 2E_{12}, \tag{2}$$

in Voigt notation (Voigt, 1910). It is noted that E_1, E_2 and E_3 are the normal strains in the 1, 2 and 3 directions, respectively and E_4, E_5 and E_6 are the shear strains in the 2-3, 1-3 and 1-2 planes, respectively. The constants C_i, C_{ij}, $C_{ijk}, \dots$ are elastic constants. Generally, the energy density U is defined per unit reference, undeformed, volume. For 2D materials, since thickness is not always uniquely defined, we define U in terms of energy per unit reference area. Therefore, the units of U used are J/m^2 which is equivalent to N/m. It follows that the elastic constants are presented as membrane elastic constants in N/m. The strain energy density W follows from Eq. (1) as

$$W = U - U_0 = C_i E_i + \frac{1}{2!} C_{ij} E_i E_j + \frac{1}{3!} C_{ijk} E_i E_j E_k + \frac{1}{4!} C_{ijkl} E_i E_j E_k E_l + \frac{1}{5!} C_{ijklm} E_i E_j E_k E_l E_m + \dots \tag{3}$$

By the hyperelastic constitutive relations in an orthonormal basis (e.g., see Slaughter (2002)), the components of the second Piola–Kirchhoff stress, $\boldsymbol{S}$, can be expressed, in Voigt notation, as

$$S_i = \frac{\partial W}{\partial E_i} = C_i + C_{ij} E_j + \frac{1}{2!} C_{ijk} E_j E_k + \frac{1}{3!} C_{ijkl} E_j E_k E_l + \frac{1}{4!} C_{ijklm} E_j E_k E_l E_m + \dots, \tag{4}$$

where S_i are the Voigt contractions of the components of the second Piola–Kirchhoff stress tensor, defined as,

$$S_1 = S_{11},\ S_2 = S_{22},\ S_3 = S_{33},\ S_4 = S_{23},\ S_5 = S_{13},\ S_6 = S_{12}. \tag{5}$$

The current work does not include prestressed materials, although the constitutive model in Eq. (4) can capture the effect of prestresses. It follows that for the undeformed state, i.e., $\boldsymbol{E} = \boldsymbol{0}$, the material is stress free, i.e., $\boldsymbol{S} = \boldsymbol{0}$, therefore,

$$C_i = 0, \quad \text{for all } i \in \{1,2,3,4,5,6\}, \tag{6}$$

and the strain energy density expansion reduces to

$$\begin{aligned} W = &\frac{1}{2!}C_{ij}E_iE_j + \frac{1}{3!}C_{ijk}E_iE_jE_k + \frac{1}{4!}C_{ijkl}E_iE_jE_kE_l \\ &+ \frac{1}{5!}C_{ijklm}E_iE_jE_kE_lE_m + \dots \end{aligned} \tag{7}$$

2.1. Plane stress constitutive model

In the case of 2D materials, we are interested in the in-plane mechanics with the out-of-plane, i.e., $\boldsymbol{e}_3$, direction left unrestrained. This corresponds to traction free boundary conditions on the top and bottom surfaces of the 2D material, i.e., plane stress boundary conditions, therefore,

$$S_3 = S_4 = S_5 = 0. \tag{8}$$

Eqs. (8) constitute a nonlinear system of three constraints. Therefore, applying these constraints to the constitutive model will allow us to express three of the strains, e.g., E_3, E_4 and E_5, as a function of the other three. We choose to let the in-plane longitudinal strain E_1, the in-plane lateral strain E_2, and the in-plane shear strain E_6 be the independent strains since we consider 2D materials and the applied deformations are in-plane. This implies that

$$\begin{aligned} W &= W\left(E_1, E_2, E_3\left(E_1, E_2, E_6\right), E_4\left(E_1, E_2, E_6\right), E_5\left(E_1, E_2, E_6\right), E_6\right) \\ &= \tilde{W}\left(E_1, E_2, E_6\right), \end{aligned} \tag{9}$$

where $\tilde{W}$ shows the change in the form of W which now depends only on the in-plane strains. In what follows, we will drop the tilde and use W to represent $\tilde{W}$ for the sake of simplicity. Following Eq. (9), the problem can be reformulated as

$$\begin{aligned} W = &\frac{1}{2!}Q_{ij}E_iE_j + \frac{1}{3!}Q_{ijk}E_iE_jE_k + \frac{1}{4!}Q_{ijkl}E_iE_jE_kE_l \\ &+ \frac{1}{5!}Q_{ijklm}E_iE_jE_kE_lE_m + \dots \end{aligned} \tag{10}$$

where $Q_{ij}, Q_{ijk}, \dots$ are the plane stress reduced elastic constants and the indices $i, j, \dots \in \{1,2,6\}$. $\boldsymbol{Q}$ has a similar mathematical structure to $\boldsymbol{C}$ for each order but with reduced matrix dimensions. We will refer to the plane stress reduced elastic constants as simply elastic constants for convenience. The second Piola–Kirchhoff stress components follow from Eq. (10) as,

$$\begin{aligned} S_i = \frac{\partial W}{\partial E_i} = &Q_{ij}E_j + \frac{1}{2!}Q_{ijk}E_jE_k + \frac{1}{3!}Q_{ijkl}E_jE_kE_l \\ &+ \frac{1}{4!}Q_{ijklm}E_jE_kE_lE_m + \dots \end{aligned} \tag{11}$$

In general, any polynomial order N_p can be used in the expansion of the strain energy density

$$W = \sum_{k=2}^{N_p} \frac{1}{k!} Q_{i_1 i_2 \dots i_k} E_{i_1} E_{i_2} \dots E_{i_k}. \tag{12}$$

It will be shown later that a 5th order expansion ($N_p = 5$) is sufficient for black phosphorus. The methodology presented in the current work for the calculation of elastic constants does not make any assumptions about the order of the expansion.

Table 1
Total number of independent plane stress reduced elastic constants to be determined for each polynomial order N_p and different material symmetries.

Polynomial order N_p	Hexagonal symmetry	Orthorhombic symmetry	Triclinic symmetry
$N_p = 2$	2	4	6
$N_p = 3$	5	10	16
$N_p = 4$	9	19	31
$N_p = 5$	14	31	52

Using the index notation, it can be shown that the plane stress reduced elastic constants satisfy the symmetry

$$Q_{a_1 \dots a_i \dots a_j \dots a_l} = Q_{a_1 \dots a_j \dots a_i \dots a_l}, \quad i, j \in \{1, 2, \dots, l\}, \tag{13}$$

for any transposition of two indices and thus any arbitrary permutation (e.g., see Pinter (1990)). Table 1 shows the total number of linearly independent plane stress reduced elastic constants that need to be determined for each material symmetry and order of the constitutive polynomial. The number of elastic constants increases with decreasing material symmetry and with increasing order of the polynomial used for the constitutive model.

Following from Eq. (13), the number of linearly independent elastic constants of order p for a triclinic material is the number of distinct solutions $\left(N_1, N_2, N_6\right)$ to the equation

$$N_1 + N_2 + N_6 = p, \tag{14}$$

where N_1, N_2 and N_6 represent the number of indices corresponding to 1, 2 and 6, respectively, in $Q_{i_1 i_2 \dots i_p}$. Therefore, for a polynomial order N_p, the total number of elastic constants to be determined for a triclinic material is given by (e.g., see Feller (1968)),

$$\sum_{p=2}^{N_p} \binom{p+3-1}{p} = \frac{1}{2}\sum_{p=2}^{N_p}\left(p^2 + 3p + 2\right). \tag{15}$$

In the case of 2D materials that exhibit symmetry, the number of independent elastic constants can be determined using character theory (e.g., see Bhagavantam and Suryanarayana (1949)).

2.2. Linearized mechanical properties

While the polynomial based constitutive model is applicable for finite deformations, in certain applications, we may be interested in the linearized mechanical properties of the material under infinitesimal deformations. The linearized mechanical properties can also be used for experimental validation under small deformations.

In the case of infinitesimal deformations, the Green–St. Venant strain tensor $\boldsymbol{E}$ reduces to the infinitesimal strain tensor $\boldsymbol{\varepsilon}$. Similarly, the second Piola–Kirchhoff stress tensor $\boldsymbol{S}$ reduces to the Cauchy stress tensor $\boldsymbol{\sigma}$. In the linear elastic regime where $\| \boldsymbol{E} \| \ll 1$, Eq. (11) reduces to,

$$\sigma_i = Q_{ij}\varepsilon_j, \tag{16}$$

since the higher powers of the infinitesimal strain components are negligible. The compliance relations (e.g., see Hyer (2009)), following from Eq. (16), can be written as,

$$\begin{Bmatrix} \varepsilon_1 \\ \varepsilon_2 \\ \varepsilon_6 \end{Bmatrix} = \begin{bmatrix} \frac{1}{Y_1} & -\frac{\nu_{21}}{Y_2} & \frac{\eta_{16}}{G} \\ -\frac{\nu_{12}}{Y_1} & \frac{1}{Y_2} & \frac{\eta_{26}}{G} \\ \frac{\eta_{61}}{Y_1} & \frac{\eta_{62}}{Y_2} & \frac{1}{G} \end{bmatrix} \begin{Bmatrix} \sigma_1 \\ \sigma_2 \\ \sigma_6 \end{Bmatrix} = \begin{bmatrix} Q_{11} & Q_{12} & Q_{16} \\ Q_{12} & Q_{22} & Q_{26} \\ Q_{16} & Q_{26} & Q_{66} \end{bmatrix}^{-1} \begin{Bmatrix} \sigma_1 \\ \sigma_2 \\ \sigma_6 \end{Bmatrix}, \tag{17}$$

where Y_i represents the Young's modulus in the ith direction, G represents the in-plane shear modulus, ν_{ij} are the Poisson's ratios, $\eta_{i6} = \varepsilon_i/\varepsilon_6$ (when only $\sigma_6 \neq 0$ and $i \in \{1,2\}$) are the coefficients of mutual influence of the first kind and $\eta_{6i} = \varepsilon_6/\varepsilon_i$ (when only $\sigma_i \neq 0$ and $i \in \{1,2\}$) are the coefficients of mutual influence of the second kind. Closed form expressions for all the linearized mechanical properties can

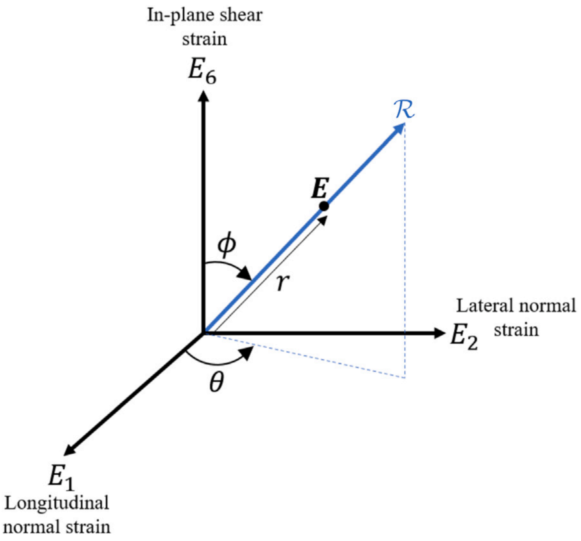

Fig. 2. A representative ray in the strain space $\mathcal{S}$.

be obtained using Eq. (17) by inverting the $\boldsymbol{Q}$ matrix. In the case of an orthorhombic material (or higher symmetry) $Q_{16} = Q_{26} = 0$, therefore, the closed form expressions for the linearized mechanical properties can be expressed in terms of the second order elastic constants as,

$$Y_1 = Q_{11} - \frac{Q_{12}^2}{Q_{22}}, \quad Y_2 = Q_{22} - \frac{Q_{12}^2}{Q_{11}}, \quad G = Q_{66}, \quad \nu_{12} = \frac{Q_{12}}{Q_{22}}, \quad \nu_{21} = \frac{Q_{12}}{Q_{11}}. \tag{18}$$

3. Ray based methodology

In the current methodology, the elastic constants of a 2D material are obtained by equating the strain energies of the crystal and that of the equivalent continuum for the same deformation. The energy calculations for the crystal are done in the atomic domain. An arbitrary 2D strain state, can be represented in Voigt notation as

$$\boldsymbol{E} = \begin{bmatrix} E_1 & E_2 & E_6 \end{bmatrix}^T, \tag{19}$$

where E_1 is the longitudinal normal strain, E_2 is the lateral normal strain and E_6 is the in-plane shear strain. Let $\mathcal{S}$ be the $\mathbb{R}^3$ space spanned by the sets of scalars E_1, E_2 and E_6. We refer to $\mathcal{S}$ as strain space. We note that $\mathcal{S}$ geometrically represents the strain states but the strain is considered as a tensor (by definition) and not a vector. In the remainder of this paper, all the deformations considered are homogeneous, and do not cause fracture, thus the resulting strains will identically satisfy the compatibility conditions. We define a strain ray $\mathcal{R}$ as a line segment, starting at the origin of $\mathcal{S}$ (under the standard $\mathbb{R}^3$ basis) and extending to any desired strain state. A ray can be uniquely identified by its azimuthal angle θ and its polar angle ϕ as shown in Fig. 2.

A point on the ray, corresponding to a strain state, can be represented by the angles defining the ray direction in addition to the Euclidean norm $r = \| \boldsymbol{E} \|$, i.e., its spherical coordinates, as

$$\begin{cases} E_1 = r \sin\phi \cos\theta \\ E_2 = r \sin\phi \sin\theta \\ E_6 = r \cos\phi \end{cases}. \tag{20}$$

The strain curve fitting range is $[0, R]$, where R represents a strain norm limit chosen to avoid non-smooth and unstable locations in the energy landscape that typically occur at large strain states. Therefore, the condition for any strain state $\boldsymbol{E}$ on a ray is $\| \boldsymbol{E} \| \leq R$, i.e., all strain states fall within the spherical domain,

$$\boldsymbol{\Sigma} = \{ \boldsymbol{E} \in \mathcal{S} \;|\; \| \boldsymbol{E} \| \leq R \}. \tag{21}$$

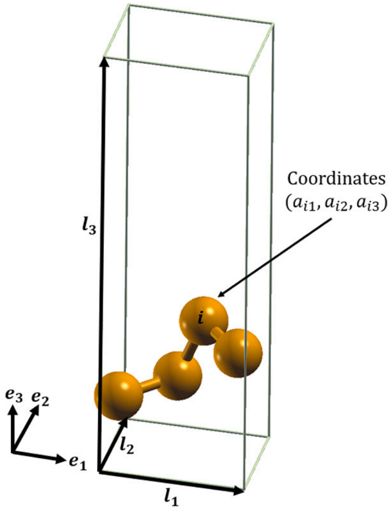

Fig. 3. Representative unit cell geometry.

We note that although a spherical domain $\boldsymbol{\Sigma}$ is used, the shape of the strain sampling region does not necessarily have to be spherical.

The subsequent formulation is independent of the methodology used for energy calculations in the atomic domain, e.g., molecular dynamics, density functional theory, etc. For a given strain state $\boldsymbol{E}$, the strain energy density is computed as,

$$W(\boldsymbol{E}) = \frac{1}{A_0} \left(\Omega_{\mathbf{E}} - \Omega_0 \right), \tag{22}$$

where $\Omega_{\mathbf{E}}$ represents the total energy for the strained state and Ω_0 is the ground state energy (undeformed state). We note that $\Omega_0 = A_0 U_0$ and $\Omega_{\mathbf{E}} = A_0 U$, U_0 and U are defined in Eq. (1). A_0 represents the area of the undeformed configuration.

The overall idea of the ray based methodology is to use linear least squares curve fitting to determine the elastic constants using a set of sampling points $\{\boldsymbol{E}\}$ in $\mathcal{S}$ and their corresponding strain energy densities $\{W\}$. The sampling points are limited to the bounded region $\boldsymbol{\Sigma}$. A ray sampling procedure in $\mathcal{S}$ was chosen because of,

1. the reduced number of energy calculations needed as compared to a conventional box sampling on a regular grid,
2. the possibility of refinement in terms of points per ray in addition to rays at different angles,
3. the computational convenience as compared to full Monte-Carlo sampling, and
4. the possibility to submit array jobs to high performance computing clusters, i.e., one array of jobs where each job corresponds to a ray which makes the computations more parallelizable.

3.1. Methodology

For a unit cell containing N_a atoms, we define $\mathscr{A}$ and $\mathscr{L}$ as respectively the matrices containing the atomic coordinates and lattice parameters of the unit cell in the form

$$\mathscr{A} = \begin{bmatrix} a_{11} & a_{21} & \dots & a_{N_a 1} \\ a_{12} & a_{22} & \dots & a_{N_a 2} \\ a_{13} & a_{23} & \dots & a_{N_a 3} \end{bmatrix}, \quad \mathscr{L} = \begin{bmatrix} l_{11} & l_{12} & l_{13} \\ l_{21} & l_{22} & l_{23} \\ l_{31} & l_{32} & l_{33} \end{bmatrix}, \tag{23}$$

where a_{ij} represents the ith atom's jth coordinate and l_{ij} represents the ith component of the jth lattice vector. An example unit cell is shown in Fig. 3.

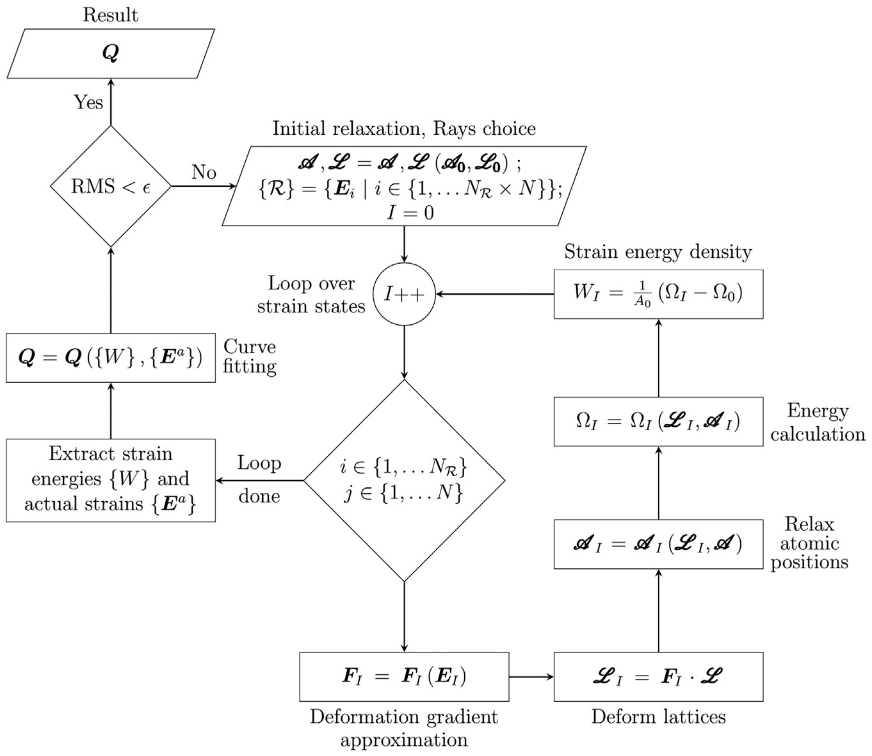

Fig. 4. Flowchart for the ray based methodology.

The underformed area A_0 in Eq. (22) can be computed using the underformed lattice vectors as

$$A_0 = \| e_{ijk}\mathscr{L}_{i1}\mathscr{L}_{j2}\boldsymbol{e}_k \|, \tag{24}$$

where $\mathscr{L}_{ij}$ are the components of the lattices matrix in the undeformed configuration, e_{ijk} represents the Levi-Civita permutation tensor (e.g., see Slaughter (2002)), $\boldsymbol{e}_k$ is the kth unit vector in the coordinate frame and $\| \cdot \|$ represents the Euclidean norm.

The unit cell, e.g., the one shown in Fig. 3, is deformed following deformation gradients corresponding to incremental strain states on different rays. This is achieved by modifying the appropriate entries in the matrix $\mathscr{L}$ and allowing the atomic coordinates to relax, i.e., updating $\mathscr{A}$, accordingly to reach a local minimum configuration in the energy landscape. The elastic constants determination procedure follows the general idea of refining by adding more rays as long as the global root mean square error (RMS) in the strain energy density is larger than a given tolerance ϵ. The condition number of the curve fitting matrices (e.g., see Golub and Van Loan (1996)) is checked to avoid ill conditioned matrices. The global logical flowchart of the ray based methodology is shown in Fig. 4. For each pair i, j labeling respectively the rays and points per ray, or equivalently the value I for the counter in Fig. 4, the strain in Voigt notation can be determined via Eq. (20) as,

$$\boldsymbol{E}_I = j\frac{R}{N}\left[\sin\phi_i\cos\theta_i \quad \sin\phi_i\sin\theta_i \quad \cos\phi_i\right]^T, \tag{25}$$

where N is the total number of strain states per ray. This follows from the fact that a ray is uniquely defined by its direction angles and a strain state is represented by its spherical coordinates in $\mathcal{S}$. Eq. (25) is based on the choice of equidistant sampling points on a ray. However, in general sampling points can be distributed arbitrarily on a ray.

The detailed procedure to find the elastic constants of a material using the ray based methodology, shown in the flowchart in Fig. 4, is as follows:

1. relax the atomic coordinates and lattice parameters to reach the ground state configuration, $\mathscr{A}$, $\mathscr{L}$,
2. retrieve the ground state energy Ω_0,
3. compute the area A_0 of the undeformed configuration from the relaxed lattice parameters,
4. define a set of $N_{\mathcal{R}}$ rays and discretize each with N corresponding strain states,
5. initiate the strain state counter $I = 1$,
6. loop over all the i and j values varying respectively over the number of rays and the number of points per ray:
    - (i) determine $\boldsymbol{E}_I$ via Eq. (25),
    - (ii) approximate and store the deformation gradient $\boldsymbol{F}_I$ given $\boldsymbol{E}_I$,
    - (iii) update the deformed lattice parameters $\mathscr{L}_I$ using $\boldsymbol{F}_I$,
    - (iv) using atomistic simulations, relax the atomic coordinates to reach the minimum energy configuration for the given deformation, i.e., update $\mathscr{A}_I$,
    - (v) retrieve the energy Ω_I for the strained state corresponding to $\mathscr{L}_I$ and $\mathscr{A}_I$ using atomistic simulations,
    - (vi) compute and store the strain energy density using Eq. (22) as $W_I = \left(\Omega_I - \Omega_0\right)/A_0$,
    - (vii) Increment I,
7. compute and store the actual strain states $\boldsymbol{E}_I^a$ corresponding to the stored deformation gradients $\boldsymbol{F}_I$,
8. given the stored actual strains $\left\{\boldsymbol{E}_I^a\right\}$ and strain energy densities $\{W\}$, check the condition numbers of the curve fitting matrices and curve fit to obtain the elastic constants $Q_{ij}, Q_{ijk}, \ldots$,
9. compute the root mean square errors. Add more rays as necessary.

The unit cell boundary conditions used are periodic in all directions with a large $\boldsymbol{l}_3$ vector, as shown in Fig. 3, to avoid interlayer interactions. This is equivalent to considering quasi-infinite crystals, i.e., studying the asymptotic behavior as the material's in-plane dimensions are much larger than its thickness. This is the case in general for 2D materials in application. This assumption can be relaxed to study finite systems by increasing the distance between the atoms in adjacent unit cells. The important aspects of the algorithmic steps are discussed in the following sections.

3.2. Rays choice

In this methodology, we choose the number and orientation of the rays and the number of strain states per ray. The specific ray directions are not very critical provided a sufficient number of rays are used. We recommend starting with uniaxial rays, i.e., only one non-vanishing strain component, e.g., E_1, then successively adding one non-vanishing strain component at a time.

Although the ray based methodology is formulated to be independent of the material symmetries, the latter can be considered when choosing the rays. The more symmetric the material is, the fewer the rays required to determine its elastic constants since symmetry will imply that some elastic constants are linearly dependent. For example, in the case of a hexagonal material, considering just a two-dimensional subspace of $\mathcal{S}$ will be sufficient, e.g., considering only longitudinal tests E_1 and E_2 and biaxial tests E_1-E_2 with no need to include E_6 due to the linear dependence of the elastic constants containing the index 6. For an orthorhombic material, the whole space $\mathcal{S}$ needs to be considered (i.e., even triaxial tests) but fewer rays will be needed as compared to a triclinic material.

3.3. Obtaining deformation gradients from strains

To calculate the strain energy density W for a given strain state $\boldsymbol{E}$ using atomistic simulations, a unit cell deformation is required. Therefore, it is necessary to determine a deformation gradient $\boldsymbol{F}$ corresponding to the given strain state $\boldsymbol{E}$. Solving for $\boldsymbol{F}$ analytically from the relation $\boldsymbol{E} = \frac{1}{2}\left(\boldsymbol{F}^T\boldsymbol{F} - \boldsymbol{I}\right)$ can be challenging for arbitrary strain states because $\boldsymbol{E}$ is a nonlinear function of $\boldsymbol{F}$ and both are tensor quantities. In this work, we present a way to approximate the deformation gradient as

$$\boldsymbol{F} = \begin{bmatrix} E_{11}+1 & 0 & 0 \\ 2E_{12} & E_{22}+1 & 0 \\ 2E_{13} & 2E_{23} & E_{33}+1 \end{bmatrix} = \begin{bmatrix} E_1+1 & 0 & 0 \\ E_6 & E_2+1 & 0 \\ 0 & 0 & 1 \end{bmatrix}. \tag{26}$$

We note that the deformation gradient approximation shown in Eq. (26) is intended to deform the lattice vectors, therefore, $E_{13} = E_{23} = E_{33} = 0$ since there is no out-of-plane strain applied on the unit cell. However, the atomic coordinates are still allowed to relax in the 3-direction and the 1-3 and 2-3 planes which induces out-of-plane normal and shear strains on the 2D material within the unit cell. It is noted that there is no unique deformation gradient for a given strain state due to invariance under rigid-body motion. The approximation shown in Eq. (26), while not unique, leads to a triangular deformation gradient matrix for convenience in deforming the unit cell. The actual or exact Green–St. Venant strain tensor corresponding to the approximated deformation gradient is, by definition,

$$\boldsymbol{E}^a = \frac{1}{2}\left(\boldsymbol{F}^T\boldsymbol{F} - \boldsymbol{I}\right). \tag{27}$$

The actual Green strains should be used for the curve fitting. It is noted that the strain correction shown in Eq. (27) causes the rays to deviate from a straight line but this does not affect the procedure or the accuracy of the results. An alternative way to obtain a deformation gradient from the strain tensor is the Cholesky decomposition of

$$\boldsymbol{F}^T\boldsymbol{F} = 2\boldsymbol{E} + \boldsymbol{I}, \tag{28}$$

which is a positive definite matrix thus yielding a unique Cholesky factorization (e.g., see Golub and Van Loan (1996)). We note that the Cholesky factorization will yield an upper triangular matrix for the deformation gradient $\boldsymbol{F}$. The Cholesky factorization process, while stable, is a numerical process which will yield some inaccuracies in the terms of $\boldsymbol{F}$. Although the aforementioned inaccuracies are minor, they might affect the simplicity of deforming the unit cell thus causing some noise in the energy outputs. Furthermore, having a closed form expression as the one shown in Eq. (26) is more efficient than the Cholesky process especially if three-dimensional deformation gradients are considered. Łepkowski (2020) presents a way to determine elastic constants of the model shown in Eq. (7) by solving analytically for the symmetric deformation gradients using matrix square roots. Determining matrix square roots analytically limits the choice of strain states and thus the applicability of the approach to materials of low symmetry. Numerically, matrix square roots are more computationally demanding than using a closed form expression. It is to be noted that the symmetric deformation gradients are not as convenient as triangular deformation gradients for the simulation cell deformations, e.g., in the case of in-plane shear, two lattice vectors will need to be deformed instead of only one.

3.4. Unit cell deformations

Due to the periodic crystalline nature of 2D materials, they can be represented as a set of periodic unit cells with certain periodicity vectors, therefore, simulating one of the unit cells is sufficient to generate results for the whole quasi-infinite crystal, and by extension its equivalent continuum. We note that the subsequent formulation is used to show that deformation of the unit cell translates smoothly into the equivalent continuum. It does not necessarily correspond to the atomic displacements at similar locations in the equivalent continuum, i.e., it is not an application of the Cauchy–Born rule (e.g., see Ericksen (2008)). The in-plane periodicity, i.e., lattice, vectors $\boldsymbol{l_1}$ and $\boldsymbol{l_2}$ of a unit cell define an $\mathbb{R}^2$ basis and thus any point $\boldsymbol{x}$ in the crystal can be represented as,

$$\boldsymbol{x} = \alpha \cdot \boldsymbol{l_1} + \beta \cdot \boldsymbol{l_2}, \tag{29}$$

where α and β are real coefficients. By extension, any vector $\boldsymbol{x}$ in the equivalent continuum can be represented using Eq. (29) (the origin of the Cartesian coordinate basis is assumed to be a point in the equivalent continuum). Therefore, the deformed vector $\boldsymbol{x}'$ under the effect of a deformation gradient $\boldsymbol{F}$ is given by,

$$\boldsymbol{x}' = \boldsymbol{F}\boldsymbol{x} = \alpha \cdot \boldsymbol{F}\boldsymbol{l_1} + \beta \cdot \boldsymbol{F}\boldsymbol{l_2}. \tag{30}$$

It follows that deforming the lattice parameters of one unit cell, will smear the deformation into the whole quasi-infinite 2D material. Therefore, a deformation gradient $\boldsymbol{F}$ acts on the crystal through,

$$\mathscr{L}' = \boldsymbol{F} \cdot \mathscr{L}, \tag{31}$$

where $\mathscr{L}$ is the lattice vectors matrix. Figs. 5, which represent a few unit cells under different prescribed deformations, show that deforming the unit cell smears the deformation periodically.

For the system to be at its minimum energy for each considered strain state (e.g., see Tadmor and Miller (2016)), the atomic coordinates need to be relaxed at every step in order for the system to reach the ground state or local minimum energy configuration given the current strain state. The strain energy densities can be calculated for a given deformation gradient using any atomistic simulation technique. In the present work, we use density functional theory to calculate the strain energies.

3.5. Curve fitting procedure

Consider a set of elastic constants of all orders represented in vector form as χ, where χ is a vector containing $\mathscr{M}$ linearly independent elastic constants that we are interested in determining through curve fitting. Given a set of $\mathscr{N}$ strain states $\left\{\boldsymbol{E}^{(i)} \mid i \in \{1, 2, \ldots, \mathscr{N}\}\right\}$, for each strain state $\boldsymbol{E}^{(\alpha)}$, the corresponding strain energy $W^{(\alpha)}$ obtained

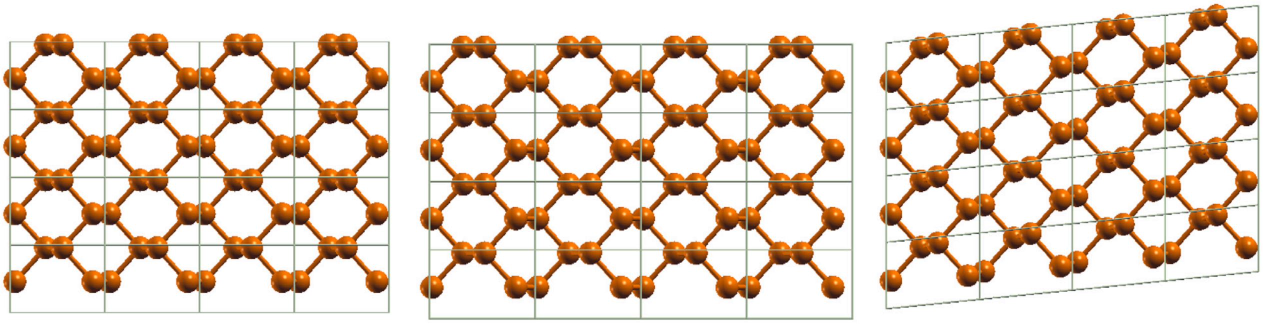
(a) Relaxed configuration (b) Longitudinal tension E_1 (c) In-plane shear E_6

Fig. 5. Unit cells subjected to different strain states.

through atomistic simulations, is equated to the strain energy from the constitutive model (10) as

$$W^{(\alpha)} = W^{(\alpha)}\left(\boldsymbol{E}^{(\alpha)}\right) = \frac{1}{2!}Q_{ij}E_i^{(\alpha)}E_j^{(\alpha)} + \frac{1}{3!}Q_{ijk}E_i^{(\alpha)}E_j^{(\alpha)}E_k^{(\alpha)} + \frac{1}{4!}Q_{ijkl}E_i^{(\alpha)}E_j^{(\alpha)}E_k^{(\alpha)}E_l^{(\alpha)} + \frac{1}{5!}Q_{ijklm}E_i^{(\alpha)}E_j^{(\alpha)}E_k^{(\alpha)}E_l^{(\alpha)}E_m^{(\alpha)} + \dots \tag{32}$$

No summation over α is implied in Eq. (32). Some terms in Eq. (32) may vanish due to the strain states considered and the latter equation can be re-arranged in matrix form in terms of the non-vanishing terms as

$$W^{(\alpha)} = \left[P(i,j) \times \frac{1}{2!}E_i^{(\alpha)}E_j^{(\alpha)} \dots P(i,j,k) \times \frac{1}{3!}E_i^{(\alpha)}E_j^{(\alpha)}E_k^{(\alpha)} \dots\right] \times \left\{Q_{ij} \quad \dots \quad Q_{ijk} \quad \dots\right\}^T, \tag{33}$$

where no summation is implied on any index and $P\left(i_1, i_2, \dots, i_n\right)$ takes into account the symmetries of the $\boldsymbol{Q}$ matrices shown in Eq. (13). P represents the number of permutations of $i_1, i_2, \dots, i_n$, which combinatorially gives

$$P\left(i_1, i_2, \dots, i_n\right) = \frac{n!}{N_1! \cdot N_2! \cdot N_6!}, \tag{34}$$

where N_1, N_2 and N_6 represent the number of indices 1, 2 and 6, respectively, in the sequence $i_1, i_2, \dots, i_n$. The system shown in Eq. (33) can be assembled in matrix form as,

$$\boldsymbol{B} \cdot \chi = \boldsymbol{W}, \tag{35}$$

where $\boldsymbol{B}$ is an $\mathscr{N} \times \mathscr{M}$ matrix whose entries are products of strain components, χ is an $\mathscr{M} \times 1$ vector of linearly independent elastic constants and $\boldsymbol{W}$ is an $\mathscr{N} \times 1$ vector of corresponding strain energy densities. If an insufficient number of independent rays, or points per ray, are used, the condition number of $\boldsymbol{B}^T\boldsymbol{B}$ may be high in which case either the generalized inverse or the Moore–Penrose pseudoinverse (e.g., see Golub and Van Loan (1996), Ben-Israel and Greville (2001) and Lawson and Hanson (1974)) can be used to solve the linear least squares system shown in Eq. (35). It is recommended to avoid such situations, since, even though the result given by the generalized inverse might replicate accurately the simulation data points, the existence of a unique solution is not necessarily guaranteed (e.g., see Ben-Israel and Greville (2001)). In order to remedy this situation, more rays or more points per ray are added to obtain a well conditioned matrix $\boldsymbol{B}^T\boldsymbol{B}$ and the resulting linear least squares problem is solved as (e.g., see Strang (1986)),

$$\chi = \left(\boldsymbol{B}^T\boldsymbol{B}\right)^{-1} \cdot \left(\boldsymbol{B}^T\boldsymbol{W}\right). \tag{36}$$

The root mean square error in the curve fit is defined as

$$\text{RMS} = \frac{\|\, \boldsymbol{W} - \boldsymbol{B} \cdot \chi \,\|}{\sqrt{\mathscr{N}}}. \tag{37}$$

It is possible to apply Eq. (36) to all the sampling points on all the rays simultaneously to obtain a global curve fit. Another approach is to apply it incrementally to different subsets of $\mathcal{S}$. Applying the equation incrementally will help decouple the system of linear equations and reduce the effect of triaxial ($E_{1,2,6} \neq 0$) curve fitting errors on biaxial and uniaxial results.

In the incremental curve fitting approach, we first curve fit for the elastic constants corresponding to the uniaxial tests sequentially. For example, given a uniaxial test where E_1 is the only non-zero strain component, then by Eq. (33), it can be seen that the only elastic constants that do not vanish are Q_{11}, Q_{111}, Q_{1111} and Q_{11111} for a fifth order polynomial expansion and therefore we solve for these constants. A similar process can be used for the other uniaxial tests. In the case of biaxial tests, the contribution of the previously determined uniaxial elastic constants to the strain energy is subtracted from the simulation energies on the right hand side of Eq. (35) to obtain the biaxial elastic constants. A similar approach is used to determine the constants corresponding to the triaxial tests. It is important to choose specific rays to be able to perform an incremental curve fit, e.g., uniaxial rays. If the rays are chosen differently, or in a way that does not follow the above procedure, we recommend global curve fitting. The ray based approach works independently of how the curve fitting is carried out.

Algorithm 1: Incremental curve fitting for the elastic constants

```
Define an ordered sequence of sets of rays (e.g., Table 2):
  $s_1, s_2, s_3, s_4, s_5, s_6, s_7$;
Assemble the linear least squares coefficients matrix $\boldsymbol{B}_i$ and the
  vector of strain energies $\boldsymbol{W}_i$ corresponding to each set of rays
  $s_i,\ i \in \{1, 2, \dots, 7\}$;
$\chi_1 = \left(\boldsymbol{B}_1^T\boldsymbol{B}_1\right)^{-1} \cdot \left(\boldsymbol{B}_1^T\boldsymbol{W}_1\right)$;
for $i \in \{2, 3, 4, 5, 6, 7\}$ do
    $\tilde{\chi} = \left[\chi_1^T\ \chi_2^T\ \dots\ \chi_{i-1}^T\right]^T$;
    $\tilde{\boldsymbol{B}} = \left[\boldsymbol{B}_1\ \boldsymbol{B}_2\ \dots\ \boldsymbol{B}_{i-1}\right]$;
    $\chi_i = \left(\boldsymbol{B}_i^T\boldsymbol{B}_i\right)^{-1} \cdot \left(\boldsymbol{B}_i^T\left[\boldsymbol{W}_i - \tilde{\boldsymbol{B}} \cdot \tilde{\chi}\right]\right)$;
end
$\chi = \left[\chi_1^T\ \chi_2^T\ \chi_3^T\ \chi_4^T\ \chi_5^T\ \chi_6^T\ \chi_7^T\right]^T$;
```

Algorithm 1 shows the exact procedure to perform an incremental curve fit. We define $s_1, s_2, \dots, s_7$ as the sets of longitudinal uniaxial, lateral uniaxial, shear uniaxial, normal biaxial, longitudinal-shear biaxial, lateral-shear biaxial and triaxial sampling rays, respectively. The geometric representation of each s_i and the form of the corresponding strain states in s_i are shown in Table 2. The incremental curve fitting process, is based on sequential curve fitting where the elastic constants determined in the previous tests, may be necessary in subsequent tests. Accordingly, the order of s_5 and s_6 is based on a lower triangular deformation gradient, e.g., Eq. (26), and the order should be swapped for an upper triangular deformation gradient, e.g., Cholesky factorization.

Table 2
Sets of rays used for incremental curve fitting to determine the elastic constants.

Set of rays	Geometric representation	Strain state
s_1	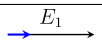	$\boldsymbol{E} = [E_1\ 0\ 0]^T$ Uniaxial longitudinal
s_2	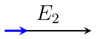	$\boldsymbol{E} = [0\ E_2\ 0]^T$ Uniaxial lateral
s_3	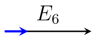	$\boldsymbol{E} = [0\ 0\ E_6]^T$ Uniaxial shear
s_4	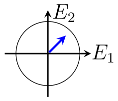	$\boldsymbol{E} = [E_1\ E_2\ 0]^T$ Biaxial normal
s_5	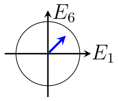	$\boldsymbol{E} = [E_1\ 0\ E_6]^T$ Biaxial longitudinal-shear
s_6	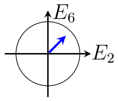	$\boldsymbol{E} = [0\ E_2\ E_6]^T$ Biaxial lateral-shear
s_7	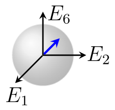	$\boldsymbol{E} = [E_1\ E_2\ E_6]^T$ Triaxial

The vector of linearly independent elastic constants determined from the rays in s_i is labeled χ_i.

In the case of materials with symmetry, e.g., hexagonal, some elastic constants may be zero and there may exist linear relations between other elastic constants. In such cases, the elastic constants can be obtained using linear least squares with equality constraints (e.g., see Lawson and Hanson (1974)).

3.6. Energy calculations

Density functional theory (DFT) (Hohenberg and Kohn, 1964; Kohn and Sham, 1965) is particularly effective for the study of the mechanical behavior of materials at the atomic scale. This follows from the Kohn–Sham assumption that the electron density varies slowly with time. This translates to an infinitesimal change in the electron density when infinitesimal strain increments are applied, and infinitesimal strain increments need to be applied to maintain thermodynamic equilibrium throughout the process. Furthermore, with the DFT periodic unit cell formulation, a small representative set of atoms can be analyzed to simulate a quasi-infinite 2D crystal.

Quantum-Espresso (Giannozzi et al., 2017, 2009) was used as a platform for the Kohn–Sham self-consistent computations to solve the Hohenberg–Kohn density functional theory equations (Kohn and Sham, 1965; Hohenberg and Kohn, 1964) using a plane-wave basis (e.g., see Tadmor and Miller (2016)). Projector augmented wave pseudopotentials (Blöchl, 1994) are used in this work to obtain accuracies comparable to using full electron potentials. The Perdew–Burke–Ernzerhof generalized gradient approximation is used (Perdew et al., 1996). We note that the generalized gradient approximation is used instead of the local-density approximation due to its higher accuracy especially when dealing with inter-atomic bond lengths (e.g., see Lee (2017)). The generalized gradient approximation is also more accurate than the local density approximation for black phosphorus (Appalakondaiah et al., 2012). The pseudopotentials we used for both graphene and black phosphorus originated from Pslibrary 1.0.0 (Dal Corso, 2014). The accuracy and precision of the pseudopotentials in Pslibrary 1.0.0 have been assessed in Lejaeghere et al. (2016) and Prandini et al. (2018).

Table 3
Converged parameter values used for Quantum-Espresso calculations.

Parameter	Graphene	Black phosphorus
K_x, K_y	20	12
K_z	2	2
Total energy convergence threshold	10^{-8} Ry	10^{-10} Ry
Electron energy convergence threshold	10^{-8} Ry	10^{-10} Ry
Force convergence threshold	10^{-8} eV/Å	10^{-8} eV/Å
Kinetic energy cut-off	150 Ry	100 Ry
z lattice vector dimension	10 Å	15 Å

Table 3 shows the Quantum-Espresso parameters used for the materials considered in this paper. K_x, K_y and K_z represent the number of points in the Monkhorst–Pack K-space sampling mesh (Monkhorst and Pack, 1976), in each reciprocal space direction, respectively. These parameters were determined using convergence analyses of the ground state energy.

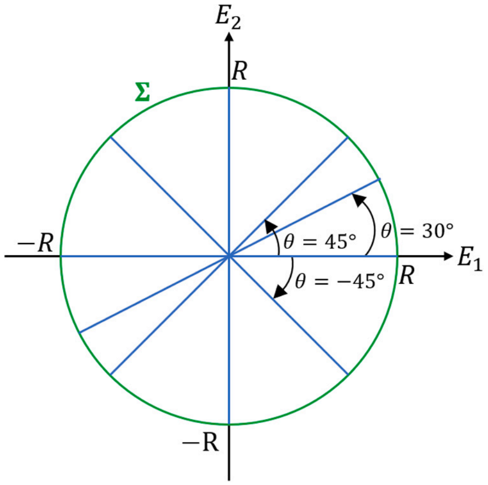

Fig. 6. Strain region used to determine the elastic constants of graphene with the rays shown in blue. (For interpretation of the references to color in this figure legend, the reader is referred to the web version of this article.)

3.7. Verification of the methodology

We assess the efficacy of the proposed ray based methodology by evaluating the elastic constants of graphene and comparing with the values published by Wei et al. (2009). It is noted that Wei et al. (2009) verified their results with the corresponding curves in Liu et al. (2007). Graphene is chosen because it is a simple hexagonal system whose elastic constants require few rays to be determined and are available in the literature (Wei et al., 2009) for comparison. Furthermore, graphene has been extensively studied in the literature (e.g., see Akinwande et al. (2017), Papageorgiou et al. (2017) and Zakharchenko et al. (2009)) and inaccurate results can be easily identified. Moreover, the unit cell size and number of electrons in graphene allow for computationally efficient refinements of the methodology. We choose a fifth order polynomial expansion of the strain energy density for comparison with (Wei et al., 2009). In the case of hexagonal symmetries, e.g., graphene, sampling rays in the E_1-E_2 subspace of S are sufficient due to linear dependence of the other constants (e.g., see Wei et al. (2009) and Cooper et al. (2013)). Therefore $\boldsymbol{\Sigma}$ is a circle of radius R in the E_1-E_2 plane. We choose $R = 0.1$ which corresponds to 10% strain and the global root mean square error tolerance $\epsilon = 10^{-3}$ J/m^2. An incremental curve fitting approach is used to determine the elastic constants. A convergence analysis is performed to assess the number of rays necessary to obtain accurate results. It is found that the rays shown in blue in Fig. 6 are sufficient to obtain accurate results. In the case of incremental curve fitting, the angles corresponding to the biaxial rays (30°, 45°, 135°, 210°, 225° and 315°) could have been

Table 4
The elastic constants of graphene.

Constant (N/m)	Ray based methodology	Wei et al. (2009)
Q_{11}	353.49	358.1
Q_{12}	62.90	60.4
Q_{111}	−2 981.66	−2 817.0
Q_{222}	−2 939.29	−2 693.3
Q_{112}	−486.43	−337.1
Q_{1111}	20 964.69	13 416.2
Q_{2222}	17 723.12	10 358.9
Q_{1112}	3 383.27	759.0
Q_{1122}	3 287.30	2 582.8
Q_{11111}	−243 000.09	−31 383.8
Q_{22222}	−126 423.34	−33 446.7
Q_{11112}	28 063.74	−88.4
Q_{12222}	−77 485.55	−13 046.6
Q_{11122}	−67 805.88	−12 960.5

chosen differently so long as a sufficient number of rays are used in conjunction with a convergence study. The elastic constants obtained using the ray based methodology are shown in Table 4 along with the results from Wei et al. (2009).

The strain energies obtained from the model with the elastic constants determined using ray based curve fitting are shown in Fig. 7 for different rays, along with the results obtained from DFT and from the model using the elastic constants determined by Wei et al. (2009). As can be seen in the figure, the results compare well with those obtained using the Wei et al. (2009) elastic constants. The global root mean square error obtained using the ray based methodology is 5.05×10^{-4} J/m^2 as compared to the value obtained using the Wei et al. (2009) elastic constants of 0.022 J/m^2. Fig. 8 shows the results for a uniaxially loaded graphene sheet. A strain E_1 is applied while keeping $S_2 = S_6 = 0$, i.e., under uniaxial stress conditions. The lateral strain E_2 is shown as predicted by the constitutive model with the elastic constants determined using the ray based methodology, with the Wei et al. (2009) elastic constants and as predicted by the DFT simulations.

We attribute the differences in the numerical results for the elastic constants between the ray based methodology and Wei et al. (2009) to the fact that they performed the curve fitting using the second Piola–Kirchhoff stresses while we used the strain energy densities. Furthermore, the Wei et al. (2009) curve fitting was done using uniaxial and equibiaxial tensile tests only, i.e., in the first quadrant of the E_1-E_2 subspace which may account for the differences shown in Fig. 8. We note that the higher order elastic constants exhibited a larger nominal difference between the ones determined using the ray based methodology as compared to the elastic constants from Wei et al. (2009). This is attributed to the high sensitivity of the higher order elastic constants on the strain range, especially that the curve fitting was done up to fracture in Wei et al. (2009), while our results were obtained in the region of strain space where strain norms are less than or equal to 10%.

Since the Wei et al. (2009) results are determined computationally using DFT, we further validate the linearized mechanical properties of graphene. Due to hexagonal symmetry, the second order elastic constants of graphene satisfy $Q_{11} = Q_{22}$ and $Q_{66} = \frac{1}{2}\left(Q_{11} - Q_{12}\right)$ (e.g., see Nye (1985)). Therefore, by Eqs. (18), $Y_1 = Y_2 = Y$, $\nu_{12} = \nu_{21} = \nu$ and $G = Y/[2(1+\nu)]$ in the linear elastic regime. Table 5 shows the linearized Young's modulus and shear modulus of graphene as calculated using Eqs. (18) and compared to the Young's modulus presented in Papageorgiou et al. (2017) and the shear modulus presented in Zakharchenko et al. (2009), respectively.

As seen in Table 5, the values compare well with the values reported in the literature. Using the values presented in the current work, the Poisson's ratio of graphene is $\nu = 0.178$.

4. Results and discussion for black phosphorus

In this section, we determine and validate the elastic constants of black phosphorus which is an orthorhombic 2D material.

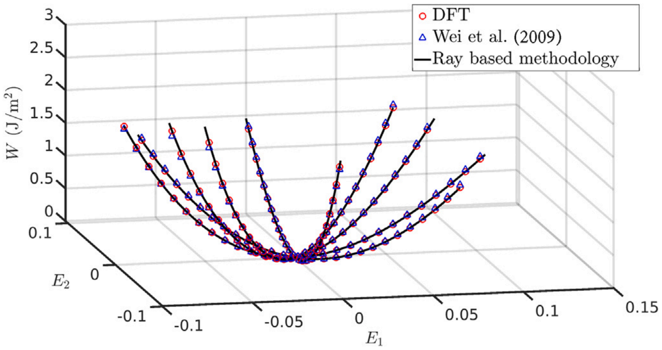

Fig. 7. Strain energy density W as a function of the in-plane normal strains E_1 and E_2 corresponding to the rays used to determine the elastic constants of graphene.

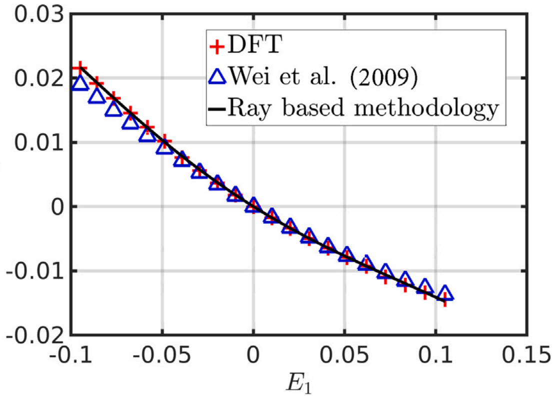

Fig. 8. Lateral normal strain E_2 induced by an applied longitudinal normal strain E_1 on a uniaxially loaded graphene sheet in the longitudinal direction.

Table 5
The linearized mechanical properties of graphene.

Elastic property	Y (N/m)	G (N/m)
Value in the current work	342.30	145.30
Value in the literature	Experimental: 340 ± 50 (Papageorgiou et al., 2017)	Monte-Carlo: 151.2 (Zakharchenko et al., 2009)

4.1. Material geometry

The relaxed black phosphorus geometry, obtained using Quantum-Espresso (Giannozzi et al., 2017, 2009), is shown in Fig. 9(a). The visualizations were done using XCrySDen (Kokalj, 1999). Fig. 9(b) shows the relaxed unit cell used for the DFT simulations. The 15 Å (15×10^{-10} m) dimension in the $\boldsymbol{e}_3$ direction is chosen to avoid any interlayer interactions resulting from the periodic boundary conditions.

Different definitions exist for the thickness of 2D materials. For example, based on the Van der Waals radius of Phosphorus (e.g., see Bondi (1964)), the thickness of black phosphorus is $t = 5.7$ Å. The subsequent results are determined independently of the thickness, e.g., the elastic constants are presented as membrane elastic constants in N/m. To obtain the elastic constants in Pa, the results should be divided by the thickness.

4.2. Material symmetry

A material is invariant under a material symmetry transformation represented by the matrix $\boldsymbol{\Gamma}$ when

$$W = W(\mathbf{E}) = W\left(\boldsymbol{\Gamma}^T \mathbf{E} \boldsymbol{\Gamma}\right), \tag{38}$$

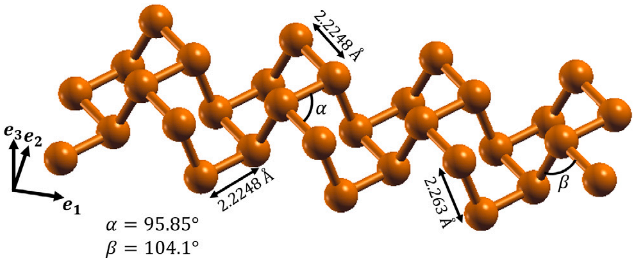

(a) Perspective view

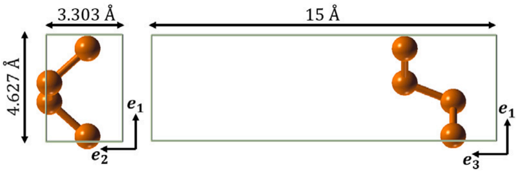

(b) Quantum-Espresso unit cell

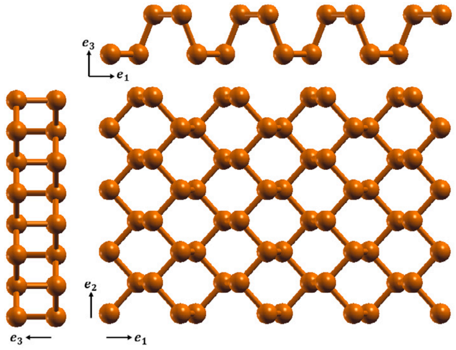

(c) Projections view

Fig. 9. Geometry of black phosphorus in its ground state.

Table 6
Orthorhombic linearly independent elastic constants for polynomial constitutive models up to fifth order.

Order of the elastic constants	Linearly independent elastic constants
Second (SOEC)	Q_{11}, Q_{12}, Q_{22}, Q_{66}
Third (TOEC)	Q_{111}, Q_{112}, Q_{122}, Q_{166}, Q_{222}, Q_{266}
Fourth (FOEC)	Q_{1111}, Q_{1112}, Q_{1122}, Q_{1166}, Q_{1222}, Q_{1266}, Q_{2222}, Q_{2266}, Q_{6666}
Fifth (FfOEC)	Q_{11111}, Q_{11112} Q_{11122}, Q_{11166}, Q_{11222}, Q_{11266}, Q_{12222}, Q_{12266}, Q_{16666}, Q_{22222}, Q_{22266}, Q_{26666}

for all $\boldsymbol{E}$. Black phosphorus is an orthorhombic 2D material thus it is invariant under the following in-plane reflection matrices

$$\boldsymbol{\Gamma}_1 = \begin{bmatrix} -1 & 0 & 0 \\ 0 & 1 & 0 \\ 0 & 0 & 1 \end{bmatrix}, \quad \boldsymbol{\Gamma}_2 = \begin{bmatrix} 1 & 0 & 0 \\ 0 & -1 & 0 \\ 0 & 0 & 1 \end{bmatrix}. \tag{39}$$

After performing the simplifications implied by Eqs. (38) and (39), only the constants presented in Table 6 are found to be linearly independent for a fifth order constitutive polynomial (and their symmetric counterparts shown in Eq. (13)). The other elastic constants are found to be identically zero due to material symmetry.

Table 7
Rays used to determine the elastic constants of black phosphorus.

Sampling ray in $\mathcal{S}$ (**E**)	$\theta(°)$	$\phi(°)$	Number of rays	Related elastic constants
$E_1 = r\cos\theta$	$\{0, 180\}$	90	2	Q_{11}, Q_{111}, Q_{1111}, Q_{11111}
$E_2 = r\sin\theta$	± 90	90	2	Q_{22}, Q_{222}, Q_{2222}, Q_{22222}
$E_6 = r\cos\phi$	0	$\{0, 180\}$	2	Q_{66}, Q_{6666}
$E_1 = r\cos\theta$, $E_2 = r\sin\theta$	$\{\pm 30, \pm 60,$ $\pm 210, \pm 240\}$	90	8	Q_{12}, Q_{112}, Q_{122}, Q_{1112}, Q_{1122}, Q_{1222}, Q_{11112}, Q_{11122}, Q_{11222}, Q_{12222}
$E_1 = r\sin\phi\cos\theta$, $E_6 = r\cos\phi$	$\{0, 180\}$	$\{30, 60\}$	4	Q_{166}, Q_{1166}, Q_{11166}, Q_{16666}
$E_2 = r\sin\phi\sin\theta$, $E_6 = r\cos\phi$	± 90	$\{30, 60\}$	4	Q_{266}, Q_{2266}, Q_{22266}, Q_{26666}
$E_1 = r\sin\phi\cos\theta$, $E_2 = r\sin\phi\sin\theta$, $E_6 = r\cos\phi$	$\{\pm 45, \pm 225\}$	45	4	Q_{1266}, Q_{11266}, Q_{12266}

4.3. *Choice of sampling rays*

Table 7 shows the ray directions used for the curve fitting, in addition to the elastic constants that are retrieved following the order of the rows through incremental curve fitting from each ray direction.

Black phosphorus, due to its orthorhombic symmetry, behaves symmetrically with respect to shear, i.e., $W\left(E_6\right) = W\left(-E_6\right)$ for any shear strain E_6, therefore more rays (or angles) were used for the E_1-E_2 subspace as compared to other biaxial tests involving shear. In Table 7, the term r is the Euclidean norm of a strain state and depends on the incremental strain step number and the number of points on each ray, i.e., it depends on the discretization of the ray considered. The bounds on r can be found based on the fact that any strain state has to be in $\boldsymbol{\Sigma}$. To determine the elastic constants of black phosphorus we choose a strain ball of radius R. Therefore, for a ray that contains N equidistant strain states,

$$r \in \left\{ j \cdot \frac{R}{N} \;\middle|\; j \in \{1, 2, \dots, N\} \right\}. \tag{40}$$

4.4. *Bounds on the curve fitting region in strain space*

The curve fitting region in strain space used to determine the elastic constants of black phosphorus is chosen to avoid non-smooth and unstable locations in the strain energy landscape. Non-smoothness occurs at strain states that correspond to points of structural degeneracies (e.g., see Mehboudi et al. (2016)) or to energy release (e.g., see Liu et al. (2016)) due to fracture. Instabilities are represented by strain states corresponding to unstable crystal structures.

It was noted in Mehboudi et al. (2016) and Barraza-Lopez et al. (2021) based on density functional theory results that black phosphorus and monochalcogenide monolayers exhibit ground state structural degeneracies. This can cause a cusp in the energy landscape as demonstrated in Mehboudi et al. (2016) and Barraza-Lopez et al. (2018). We analyzed the energy landscape for black phosphorus to identify structural degeneracies. Point A in Fig. 10 represents the ground state configuration considered in the current work (Fig. 9). Point A' corresponds to a 90° rotation about the $\boldsymbol{e}_3$ axis (Fig. 9) of the configuration represented by point A. The strain energy density is plotted along the ray starting at point A and going to point A' in Fig. 10, and vice-versa. We note that in Fig. 10, the strain energy is plotted as a function of l_{11} and l_{22} which represent the in-plane lattice parameters. In both ray

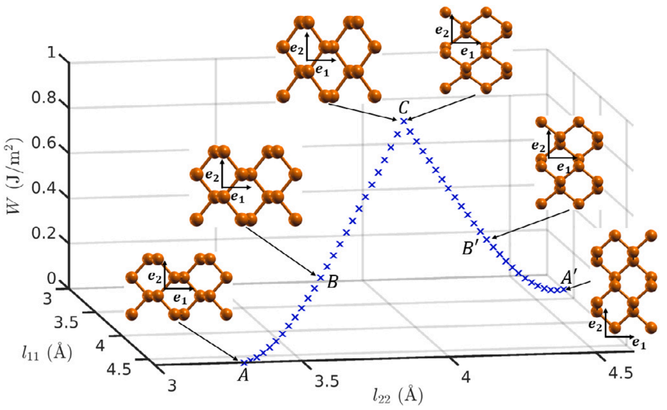

Fig. 10. Cusp in the energy landscape of black phosphorus caused by the degeneracies in its ground state.

directions, the strain energy values match for the same location in the l_{11}-l_{22} plane. A cusp can be seen along both rays at point C in Fig. 10, where two configurations have the same lattice parameters $l_{11} = l_{22}$ although one is a 90° rotation of the other. At the intermediate points having the same energy on either side of the cusp, e.g., points B and B', the corresponding configuration are 90° rotations of one another. The cusp in Fig. 10 corresponds to a strain norm of 25.74%. When using the ray based methodology the presence of non-smooth locations will affect the accuracy of the obtained elastic constants and therefore the strain space sampling region should be chosen to avoid them based on the starting ground state. The ray based methodology can be employed to determine the elastic constants of black phosphorus whether starting from point A or A' as long as the cusp is not included in the curve fitting region. It is noted that at each of the points A and A', there are two corresponding degenerate ground states which are 180° rotations of one another (e.g., see Mehboudi et al. (2016)).

The experimental range used to study the mechanical behavior of 2D materials typically includes some nonlinear behavior. For example, in Huang et al. (2010) the range $[-3\%, 4\%]$ is used to study graphene using Raman spectroscopy. The rupture strain of a few layers of black phosphorus has been determined using atomic force microscopy to be about 9.2% in tension (Tao et al., 2015). The latter rupture limit is based on a linearized elasticity formulation, i.e., using $\sigma = Y\varepsilon$ where ε is the infinitesimal strain, which underestimates nonlinear tensile strains. Furthermore, it is based on a few layers of black phosphorus in experimental settings. Accounting for experimental variability, in the present work, we have chosen a strain ball of radius $R = 0.1$ which is equivalent to 10% strain norm. Our DFT simulations of black phosphorus did not exhibit fracture behaviors under uniaxial strain and uniaxial stress states in the strain range of $[-10\%, 10\%]$.

4.5. Elastic constants of black phosphorus

The converged elastic constants of black phosphorus, with a global root mean square error tolerance $\epsilon = 5 \times 10^{-4}$ J/m^2, are presented in Table 8. Table A.1 in the Appendix shows the curve fitting results for different numbers of points per ray to assess convergence. It is to be noted that the DFT simulations were all performed with a 40 points per ray discretization, i.e., $N = 40$, but then some points were suppressed when performing convergence studies on the number of points per ray. This is due to the fact that the closer the points in strain space, the quicker the DFT convergence because deformation is performed in smaller increments.

Figs. 11 and 12 show the strain energy curves for black phosphorus subjected to different strain states. Graphically, it can be seen that the model predictions match well with the DFT calculations.

Table 8
The converged elastic constants of black phosphorus.

Constant	Value (N/m)
Q_{11}	23.89
Q_{22}	101.95
Q_{12}	16.99
Q_{66}	22.37
Q_{111}	−177.09
Q_{222}	−1 039.50
Q_{112}	−152.04
Q_{122}	−32.49
Q_{266}	−75.05
Q_{166}	−175.66
Q_{1111}	1 537.03
Q_{2222}	9 256.02
Q_{6666}	−687.48
Q_{1112}	1 332.64
Q_{1222}	−253.71
Q_{1122}	383.97
Q_{2266}	262.38
Q_{1166}	2 458.17
Q_{1266}	950.56
Q_{11111}	−7 882.14
Q_{22222}	−102 580.02
Q_{11112}	−4 038.05
Q_{12222}	2 125.45
Q_{11122}	−4 021.55
Q_{11222}	1 108.82
Q_{22266}	−3 318.22
Q_{26666}	14 830.50
Q_{11166}	−24 868.42
Q_{16666}	−2 816.63
Q_{11266}	−14 721.49
Q_{12266}	−3 337.54

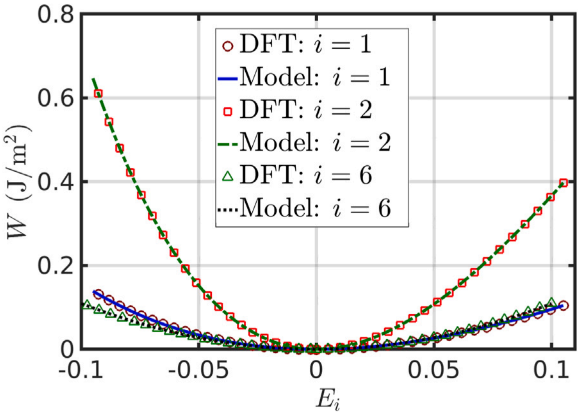

Fig. 11. Strain energy density W for the uniaxial simulations of black phosphorus.

To assess the convergence of the elastic constants with respect to the number of points per ray, we compare the Frobenius norms of matrices corresponding to the same order of the elastic constants for different numbers of points per ray. Since some small values of the elastic constants may have less effect on the strain energy density, we compare the norms of the matrices corresponding to elastic constants of different orders. The Frobenius norm (e.g., see Golub and Van Loan (1996)) is defined for a general multidimensional matrix by

$$\| \boldsymbol{M} \|_F = \sqrt{\sum_{i_1=1}^{N_{i_1}} \sum_{i_2=1}^{N_{i_2}} \cdots \sum_{i_m=1}^{N_{i_m}} M^2_{i_1 i_2 \ldots i_m}}, \tag{41}$$

where the matrix $\boldsymbol{M}$ has m dimensions and N_{i_j} are the number of elements of $\boldsymbol{M}$ in the i_j^{th} dimension.

Table 9 shows convergence of the elastic constants. The Frobenius norms of the difference between the matrices of the elastic constants for different numbers of points per ray and the corresponding matrix

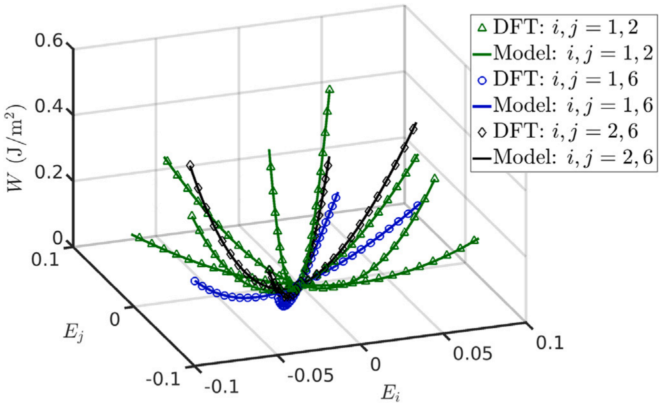

Fig. 12. Strain energy density W for the biaxial simulations of black phosphorus.

Table 9
Convergence of the Frobenius norms of different orders of the elastic constant matrices for black phosphorus.

Constants order	Frobenius norm (N/m) for 40 points per ray	Difference (%) between 5 and 40 points per ray	Difference (%) between 10 and 40 points per ray	Difference (%) between 20 and 40 points per ray
SOEC	109.74	0.028	0.018	0.0068
TOEC	1 137.50	0.083	0.021	0.0069
FOEC	12 011.09	0.71	0.40	0.15
FfOEC	158 532.80	1.26	0.51	0.20

for 40 points per ray decreases as the number of points increases. Since analytically the elastic constants are,

$$\left.\frac{\partial^2 W}{\partial E_i \partial E_j}\right|_{\boldsymbol{E}=\boldsymbol{0}} = Q_{ka}\delta_{ki}\delta_{aj} = Q_{ij}, \quad \left.\frac{\partial^3 W}{\partial E_i \partial E_j \partial E_k}\right|_{\boldsymbol{E}=\boldsymbol{0}} = Q_{ijk}, \dots, \tag{42}$$

the convergence is faster for the lower order constants because higher order constants are more sensitive to minor differences in strain energy. The sensitivity of higher order constants follows from the fact that differentiation of numerical results will amplify the noise/error. Table 10 shows the convergence of the global root mean square error (RMS) of the strain energies.

4.6. *Effect of the order of the constitutive polynomial*

In this section, the order of the constitutive polynomial required to compute accurate strain energies for black phosphorus is assessed. The order of the constitutive polynomial is defined as the order of the highest power of the strains in the constitutive polynomial, i.e., N_p in Eq. (12), e.g.,

$$\begin{aligned}
\text{Second order } (N_p = 2): \quad W &= \frac{1}{2!}Q_{ij}E_iE_j, \\
\text{Third order } (N_p = 3): \quad W &= \frac{1}{2!}Q_{ij}E_iE_j + \frac{1}{3!}Q_{ijk}E_iE_jE_k, \\
\text{Fourth order } (N_p = 4): \quad W &= \frac{1}{2!}Q_{ij}E_iE_j + \frac{1}{3!}Q_{ijk}E_iE_jE_k \\
&\quad + \frac{1}{4!}Q_{ijkl}E_iE_jE_kE_l, \qquad (43)\\
\text{Fifth order } (N_p = 5): \quad W &= \frac{1}{2!}Q_{ij}E_iE_j + \frac{1}{3!}Q_{ijk}E_iE_jE_k \\
&\quad + \frac{1}{4!}Q_{ijkl}E_iE_jE_kE_l \\
&\quad + \frac{1}{5!}Q_{ijklm}E_iE_jE_kE_lE_m.
\end{aligned}$$

Table A.2 in the Appendix shows the elastic constants for varying polynomial orders ranging from second to fifth. Figs. 13 show the effects of different orders of the constitutive polynomial on the uniaxial strain energy curves for black phosphorus. Table 11 shows the global root mean square errors for different polynomial orders. It can be seen in Table 11 that with increasing order of the polynomial, the curve fitting is more accurate, i.e., the global root mean square error decreases. It is found that a fifth order polynomial expansion is sufficient to accurately determine the strain energies of black phosphorus for strain state norms less than or equal to 10%.

Table 10
Convergence of the global root mean square error in the curve fit to determine the elastic constants of black phosphorus with respect to the number of points per ray.

Points per ray	5 points	10 points	20 points	40 points
Global RMS error (J/m^2)	6×10^{-4}	5.3×10^{-4}	4.93×10^{-4}	4.73×10^{-4}

Table 11
Convergence of the global root mean square error in the curve fit to determine the elastic constants of black phosphorus with the order of the constitutive polynomial used.

Order of the polynomial used	Second ($N_p = 2$)	Third ($N_p = 3$)	Fourth ($N_p = 4$)	Fifth ($N_p = 5$)
Global RMS error (J/m^2)	0.0334	0.0027	6.8×10^{-4}	4.73×10^{-4}

Table 12
Additional rays to verify that the number of rays used for the curve fitting to determine the elastic constants of black phosphorus is sufficient.

$\theta(°)$	± 90	$\{0, 180\}$	$\pm\{30, 210\}$	$\pm\{15, 45, 75, 195, 225, 255\}$
$\phi(°)$	45	45	$\{30, 60\}$	90
Number of rays	2	2	8	12

4.7. *Verification studies*

In order to verify that a sufficient number of rays are used for the curve fitting process, the strain energy density of five strain states on each of the rays shown in Table 12 is determined using DFT and compared to the corresponding model prediction. It is to be noted that the rays shown in Table 12 were not used to curve fit for the elastic constants of black phosphorus. The global root mean square error obtained from the comparison is 4.6×10^{-4} J/m^2, which shows that the constitutive model with the determined elastic constants predicts accurately strain energies for other strains within $\boldsymbol{\Sigma}$.

The next verification study consists of conducting uniaxial stress simulations and comparing the DFT stresses with the stresses predicted by the constitutive model. A uniaxial stress simulation in the 1-direction is equivalent to applying a strain E_1 to the DFT unit cell while keeping $S_2 = S_6 = 0$, i.e., allowing the material to contract laterally and to shear. The Newton–Raphson method (e.g., see Allen-I.I.I. and Isaacson (1998)), with a tolerance of 10^{-6}, is used to solve the system of nonlinear equations generated by the model (11) from the boundary conditions $S_2 = S_6 = 0$ given an applied strain E_1, i.e., solving for E_2 and E_6. The indicial stress derivative relation, which is used in the Newton–Raphson algorithm, is

$$\frac{\partial S_\tau}{\partial E_\alpha} = Q_{\tau\alpha} + Q_{\tau\alpha k}E_k + \frac{1}{2!}Q_{\tau\alpha jk}E_jE_k + \frac{1}{3!}Q_{\tau\alpha ijk}E_iE_jE_k. \tag{44}$$

Fig. 14(a) shows the induced E_2 as a function of the applied strain E_1 as predicted by the model and as calculated using DFT, where the material is subjected to the boundary conditions $S_2 = S_6 = 0$. As can be seen, the model predictions match well with the DFT calculations with a root mean square error of 6.32×10^{-5}. Using a similar process, E_1, for a uniaxial stress loading in the 2-direction, is evaluated as a function of E_2 and is shown in Fig. 14(b). The corresponding root mean square error is 0.0012.

Fig. 15(a) shows the nonlinear stress–strain curves obtained from DFT and predicted by the constitutive model for a uniaxial stress simulation in the 1-direction. The stress S_1 is calculated using the determined E_2 and E_6 and the applied E_1 in Eq. (11). As can be seen,

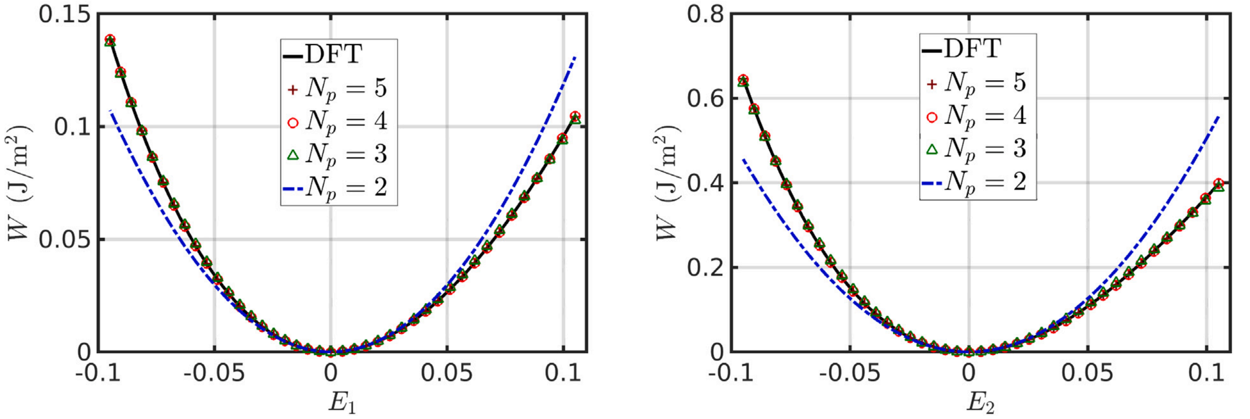

(a) Strain energy density W vs. the longitudinal strain E_1

(b) Strain energy density W vs. the lateral strain E_2

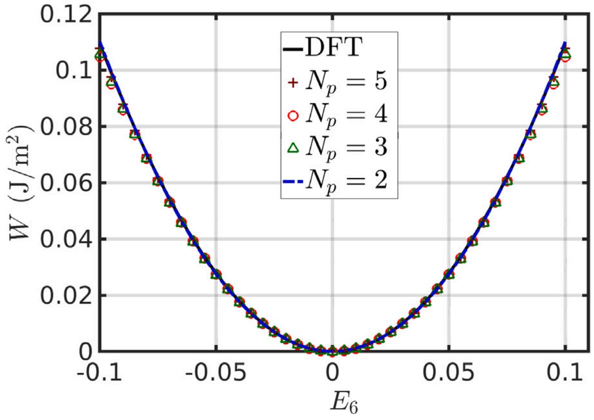

(c) Strain energy density W vs. the shear strain E_6

Fig. 13. Effect of the order of the constitutive polynomial on the uniaxial strain energy curves of black phosphorus.

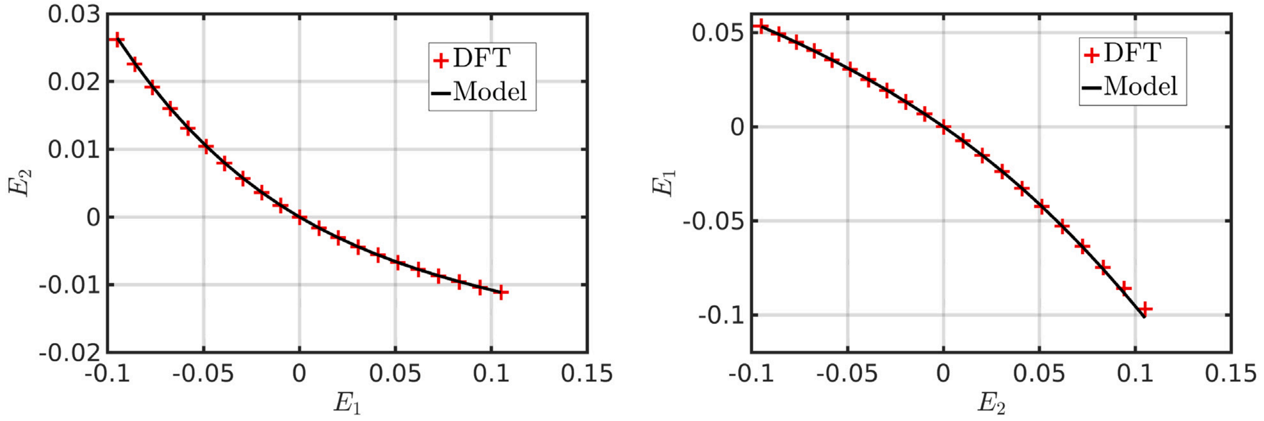

(a) Lateral strain E_2 induced by an applied longitudinal strain E_1

(b) Longitudinal strain E_1 induced by an applied lateral strain E_2

Fig. 14. Normal strains induced by uniaxial normal stress loadings of black phosphorus.

the predicted stresses match well with the DFT stresses, with a root mean square error of 0.006 N/m. Using a similar process, the stress–strain curves for the uniaxial stress in the 2-direction and shear were generated and are shown in Fig. 15(b) and Fig. 15(c), respectively. The root mean square errors obtained are 0.017 N/m for the uniaxial stress in the 2-direction and 0.071 N/m for the uniaxial shear stress simulation. Higher root mean square errors are noticed in the stresses as compared to strain energies, which can be attributed to the fact that stress, which involves differentiating strain energy, amplifies numerical errors and inaccuracies. The uniaxial shear stress simulation exhibits

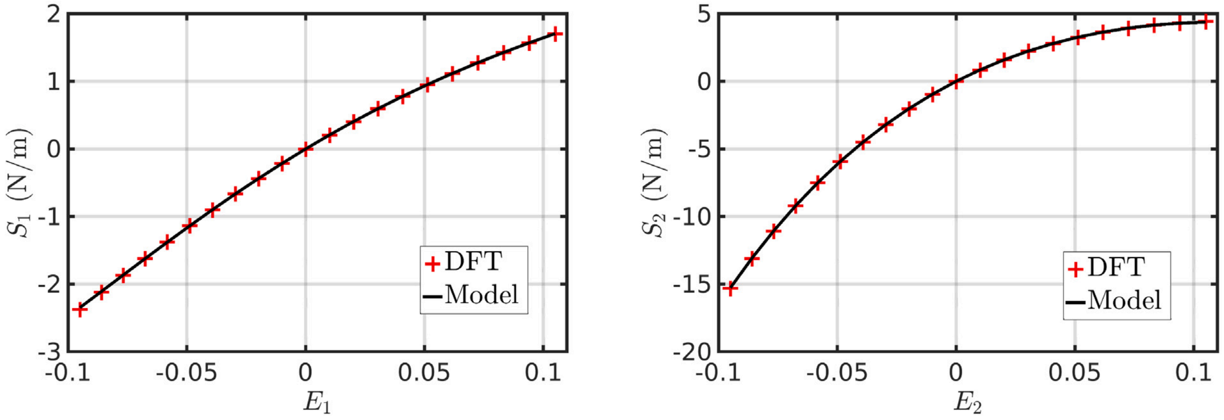

(a) Longitudinal stress S_1 vs. strain E_1

(b) Lateral stress S_2 vs. strain E_2

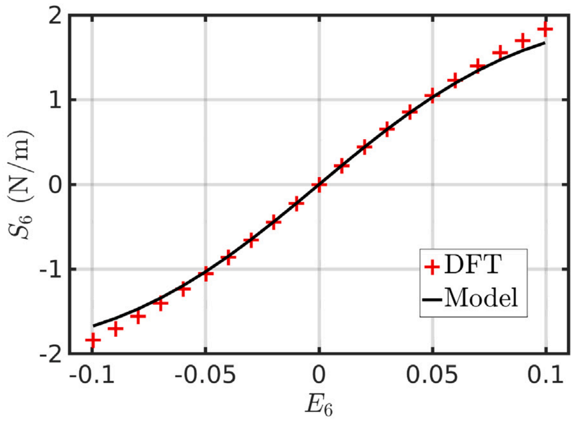

(c) Shear stress S_6 vs. strain E_6

Fig. 15. Stress–strain curves corresponding to the uniaxial stress loadings of black phosphorus.

Table 13
The linearized mechanical properties of black phosphorus in comparison with Wang et al. (2015).

Elastic property	Y_1 (N/m)	Y_2 (N/m)	ν_{12}	ν_{21}	G (N/m)
Current value	21.06	89.87	0.167	0.711	22.37
Value in Wang et al. (2015)	23.0	92.3	0.175	0.703	22.4
Difference (%)	9.2	2.7	4.79	1.11	0.13

a higher root mean square error which follows from the fact that shear strains, especially nonlinear shear strains, induce longitudinal strains E_1 and E_2 for an orthorhombic material, therefore the effect of higher order triaxial elastic constants, e.g., Q_{1266}, is more pronounced for larger strains. This effect does not happen in the uniaxial normal stress simulations since for an orthorhombic material, E_1 and E_2 do not induce E_6. The root mean square error can be further reduced by adding more triaxial rays, i.e., $E_{1,2,6} \neq 0$.

Table 13 shows the linearized mechanical properties of black phosphorus calculated using Eqs. (18) in comparison with the results presented in Wang et al. (2015). We note that Y_1, Y_2 and G represent the slope at the origin in Fig. 15(a), 15(b) and 15(c), respectively. The Poisson's ratios ν_{12} and ν_{21} represent the slope at the origin in Figs. 14(a) and 14(b), respectively. These slopes when calculated using finite differences, compare well with the values presented in Table 13.

The differences shown in Table 13 may be attributed to differences in the parameters used for the DFT simulations. In addition, in Wang et al. (2015), the results were obtained solely based on infinitesimal deformations, whereas in the present work the results are deduced from a general nonlinear elastic model.

5. Conclusion

Murnaghan's polynomial based constitutive model has been effectively used in the literature to model the nonlinear elastic response of 2D materials of hexagonal symmetry using a fifth order expansion. However, an increasing number of elastic constants need to be determined for 2D materials of lower symmetry and higher polynomial orders. In this paper, a general methodology to determine the elastic constants is presented for 2D materials of arbitrary symmetries and constitutive polynomials of any order. The methodology is based on ray sampling of the strain energy density in a bounded region of strain space and curve fitting to obtain the plane stress reduced elastic constants. The proposed methodology is not based on any assumption about the energy calculation approach. While DFT is employed in the current work, any energy calculation method can be used with the methodology. The ray based methodology is presented algorithmically and is verified by comparing the results for graphene with those available in the literature. Subsequently, the methodology is used to determine the elastic constants of black phosphorus up to fifth order. Convergence and error analyses are used to assess the validity of the determined elastic constants. The effect of the order of the constitutive polynomial on the elastic constants of black phosphorus is assessed. Additionally, the linearized mechanical properties of black phosphorus are evaluated and compared with the literature.

Table A.1
The elastic constants of black phosphorus for different numbers of curve fitting points per ray.

Constant (N/m)	5 points	10 points	20 points	40 points
Q_{11}	23.89	23.89	23.89	23.89
Q_{22}	101.92	101.93	101.94	101.95
Q_{12}	16.99	16.99	16.99	16.99
Q_{66}	22.37	22.37	22.37	22.37
Q_{111}	−176.88	−176.94	−177.03	−177.09
Q_{222}	−1 039.34	−1 039.44	−1 039.48	−1 039.50
Q_{112}	−151.90	−151.97	−152.02	−152.04
Q_{122}	−32.54	−32.49	−32.49	−32.49
Q_{266}	−75.55	−75.13	−75.06	−75.05
Q_{166}	−175.65	−175.66	−175.66	−175.66
Q_{1111}	1 542.70	1 540.56	1 538.39	1 537.03
Q_{2222}	9 325.53	9 297.49	9 271.80	9 256.02
Q_{6666}	−686.80	−687.06	−687.33	−687.48
Q_{1112}	1 322.62	1 327.02	1 330.55	1 332.64
Q_{1222}	−255.10	−254.89	−254.20	−253.71
Q_{1122}	380.34	383.34	383.91	383.97
Q_{2266}	253.08	259.33	261.49	262.38
Q_{1166}	2 469.69	2 464.05	2 460.30	2 458.17
Q_{1266}	957.83	954.16	951.85	950.56
Q_{11111}	−8 584.52	−8 354.59	−8 073.94	−7 882.14
Q_{22222}	−103 538.04	−103 060.32	−102 754.93	−102 580.02
Q_{11112}	−3 990.24	−4 007.83	−4 027.34	−4 038.05
Q_{12222}	2 073.61	2 060.47	2 095.88	2 125.45
Q_{11122}	−4 006.68	−4 049.81	−4 037.72	−4 021.55
Q_{11222}	936.71	1 020.59	1 076.16	1 108.82
Q_{22266}	−3 034.13	−3 290.65	−3 323.76	−3 318.22
Q_{26666}	15 254.91	14 827.25	14 800.32	14 830.50
Q_{11166}	−24 972.92	−24 926.65	−24 890.63	−24 868.42
Q_{16666}	−2 984.39	−2 898.47	−2 847.20	−2 816.63
Q_{11266}	−14 618.57	−14 700.99	−14 718.45	−14 721.49
Q_{12266}	−3 349.05	−3 348.50	−3 342.35	−3 337.54

Table A.2
The elastic constants of black phosphorus for different constitutive polynomial orders.

Constant (N/m)	$N_p = 2$	$N_p = 3$	$N_p = 4$	$N_p = 5$
Q_{11}	23.75	24.82	23.92	23.89
Q_{22}	101.05	107.47	102.23	101.95
Q_{12}	16.77	17.65	17.03	16.99
Q_{66}	21.95	21.95	22.37	22.37
Q_{111}	–	−176.57	−180.15	−177.09
Q_{222}	–	−1 058.55	−1 079.30	−1 039.50
Q_{112}	–	−150.26	−148.07	−152.04
Q_{122}	–	−35.28	−33.18	−32.49
Q_{266}	–	−73.34	−65.42	−75.05
Q_{166}	–	−175.82	−188.71	−175.66
Q_{1111}	–	–	1 489.24	1 537.03
Q_{2222}	–	–	8 633.84	9 256.02
Q_{6666}	–	–	−687.52	−687.48
Q_{1112}	–	–	1 268.63	1 332.64
Q_{1222}	–	–	−251.24	−253.71
Q_{1122}	–	–	342.78	383.97
Q_{2266}	–	–	231.47	262.38
Q_{1166}	–	–	2 379.85	2 458.17
Q_{1266}	–	–	862.52	950.56
Q_{11111}	–	–	–	−7 882.14
Q_{22222}	–	–	–	−102 580.02
Q_{11112}	–	–	–	−4 038.05
Q_{12222}	–	–	–	2 125.45
Q_{11122}	–	–	–	−4 021.55
Q_{11222}	–	–	–	1 108.82
Q_{22266}	–	–	–	−3 318.22
Q_{26666}	–	–	–	14 830.50
Q_{11166}	–	–	–	−24 868.42
Q_{16666}	–	–	–	−2 816.63
Q_{11266}	–	–	–	−14 721.49
Q_{12266}	–	–	–	−3 337.54

CRediT authorship contribution statement

Serge R. Maalouf: Conceptualization, Methodology, Software, Validation, Formal analysis, Data curation, Writing – original draft, Writing – review & editing. **Senthil S. Vel:** Conceptualization, Methodology, Software, Validation, Formal analysis, Writing – original draft, Writing – review & editing, Supervision.

Declaration of competing interest

The authors declare that they have no known competing financial interests or personal relationships that could have appeared to influence the work reported in this paper.

Acknowledgments

The computational work required for this paper was done in part on the Extreme Science and Engineering Discovery Environment (XSEDE) (Towns et al., 2014), which is supported by National Science Foundation, USA, under the startup grant TG-MSS180013. The other part of the computational work was done on the University of Maine System Advanced Computing Group (ACG) clusters. The authors would like to express their gratitude to Mr. Stephen Cousins at the University of Maine System Advanced Computing Group who helped with cluster issues and implementations. We would also like to thank the anonymous reviewers for their constructive suggestions.

Appendix. Convergence tables

See Tables A.1 and A.2.

References

Ahmadi, A., Masoudi, M., Taghizade, N., Jafari, H., Faghihnasiri, M., 2019. Study of mechanical and electronic properties of single-layer FeB2. Phys. E Low Dimens. Syst. Nanostruct. 112, 71–77.

Akinwande, D., Brennan, C.J., Bunch, J.S., Egberts, P., Felts, J.R., Gao, H., Huang, R., Kim, J.-S., Li, T., Li, Y., Liechti, K.M., Lu, N., Park, H.S., Reed, E.J., Wang, P., Yakobson, B.I., Zhang, T., Zhang, Y.-W., Zhou, Y., Zhu, Y., 2017. A review on mechanics and mechanical properties of 2D materials—Graphene and beyond. Extreme Mech. Lett. 13, 42–77.

Allen-I.I.I., M.B., Isaacson, E.L., 1998. Numerical Analysis for Applied Sciences, first ed. John Wiley & Sons Inc., Hoboken.

Appalakondaiah, S., Vaitheeswaran, G., Lebègue, S., Christensen, N.E., Svane, A., 2012. Effect of van der Waals interactions on the structural and elastic properties of black phosphorus. Phys. Rev. B 86 (3), 035105.

Barraza-Lopez, S., Fregoso, B.M., Villanova, J.W., Parkin, S.S.P., Chang, K., 2021. Colloquium: Physical properties of group-IV monochalcogenide monolayers. Rev. Modern Phys. 93, 011001. http://dx.doi.org/10.1103/RevModPhys.93.011001.

Barraza-Lopez, S., Kaloni, T.P., Poudel, S.P., Kumar, P., 2018. Tuning the ferroelectric-to-paraelectric transition temperature and dipole orientation of group-IV monochalcogenide monolayers. Phys. Rev. B 97, 024110. http://dx.doi.org/10.1103/PhysRevB.97.024110.

Ben-Israel, A., Greville, T.N.E., 2001. Generalized Inverses: Theory and Applications, second ed. Wiley, New York.

Bhagavantam, S., Suryanarayana, D., 1949. Crystal symmetry and physical properties: application of group theory. Acta Crystallogr. 2 (1), 21–26.

Birch, F., 1947. Finite elastic strain of cubic crystals. Phys. Rev. 71, 809–824.

Blöchl, P., 1994. Projector augmented-wave method. Phys. Rev. B 50 (24), 17953–17979.

Bondi, A., 1964. van der Waals volumes and radii. J. Phys. Chem. 68 (3), 441–451.

Cadelano, E., Palla, P.L., Giordano, S., Colombo, L., 2009. Nonlinear elasticity of monolayer graphene. Phys. Rev. Lett. 102 (23), 235502.

Cao, P., Wu, J., Zhang, Z., Ning, F., 2017. Mechanical properties of monocrystalline and polycrystalline monolayer black phosphorus. Nanotechnology 28 (4), 045702.

Chen, H., Huang, P., Guo, D., Xie, G., 2016. Anisotropic mechanical properties of black phosphorus nanoribbons. J. Phys. Chem. C 120 (51), 29491–29497.

Cooper, R.C., Lee, C., Marianetti, C.A., Wei, X., Hone, J., Kysar, J.W., 2013. Nonlinear elastic behavior of two-dimensional molybdenum disulfide. Phys. Rev. B 87, 035423.

Dal Corso, A., 2014. Pseudopotentials periodic table: From H to Pu. Comput. Mater. Sci. 95, 337–350. http://dx.doi.org/10.1016/j.commatsci.2014.07.043.

Davydov, S.Y., 2011. Third-order elastic moduli of single-layer graphene. Phys. Solid State 53 (3), 665–668.

Du, H., Lin, X., Xu, Z., Chu, D., 2015. Recent developments in black phosphorus transistors. J. Mater. Chem. C 3, 8760–8775.

Ericksen, J., 2008. On the Cauchy—Born rule. Math. Mech. Solids 13 (3–4), 199–220. http://dx.doi.org/10.1177/1081286507086898.

Faghihnasiri, M., Jafari, H., Ramazani, A., Shabani, M., Estalaki, S.M., Larson, R.G., 2019. Nonlinear elastic behavior and anisotropic electronic properties of two-dimensional borophene. J. Appl. Phys. 125 (14), 145107.

Feller, W., 1968. An Introduction to Probability Theory and Its Applications, Vol. 1, third ed. John Wiley & Sons Inc., Hoboken, p. 38.

Fish, J., Chen, W., Li, R., 2007. Generalized mathematical homogenization of atomic media at finite temperatures in three dimensions. Comput. Method Appl. M. 196 (4), 908–922. http://dx.doi.org/10.1016/j.cma.2006.08.001.

Fisher, D.J., 2018. Rhenium Disulfide, first ed. Materials Research Forum LLC, Millersville.

Ghaffari, R., Shirazian, F., Hu, M., Sauer, R.A., 2019. A nonlinear hyperelasticity model for single layer blue phosphorus based on ab initio calculations. Proc. Roy. Soc. A-Math. Phy. 475 (2229), 20190149.

Giannozzi, P., Andreussi, O., Brumme, T., Bunau, O., Nardelli, M.B., Calandra, M., Car, R., Cavazzoni, C., Ceresoli, D., Cococcioni, M., Colonna, N., Carnimeo, I., Dal Corso, A., de Gironcoli, S., Delugas, P., Jr, R.A.D., Ferretti, A., Floris, A., Fratesi, G., Fugallo, G., Gebauer, R., Gerstmann, U., Giustino, F., Gorni, T., Jia, J., Kawamura, M., Ko, H.-Y., Kokalj, A., cükbenli, E.K., Lazzeri, M., Marsili, M., Marzari, N., Mauri, F., Nguyen, N.L., Nguyen, H.-V., de-la Roza, A.O., Paulatto, L., Poncé, S., Rocca, D., Sabatini, R., Santra, B., Schlipf, M., Seitsonen, A.P., Smogunov, A., Timrov, I., Thonhauser, T., Umari, P., Vast, N., Wu, X., Baroni, S., 2017. Advanced capabilities for materials modelling with QUANTUM ESPRESSO. J. Phys. Condens. Matter 29 (46), 465901, URL http://stacks.iop.org/0953-8984/29/i=46/a=465901.

Giannozzi, P., Baroni, S., Bonini, N., Calandra, M., Car, R., Cavazzoni, C., Ceresoli, D., Chiarotti, G.L., Cococcioni, M., Dabo, I., Dal Corso, A., de Gironcoli, S., Fabris, S., Fratesi, G., Gebauer, R., Gerstmann, U., Gougoussis, C., Kokalj, A., Lazzeri, M., Martin-Samos, L., Marzari, N., Mauri, F., Mazzarello, R., Paolini, S., Pasquarello, A., Paulatto, L., Sbraccia, C., Scandolo, S., Sclauzero, G., Seitsonen, A.P., Smogunov, A., Umari, P., Wentzcovitch, R.M., 2009. QUANTUM ESPRESSO: A modular and open-source software project for quantum simulations of materials. J. Phys. Condens. Matter 21 (39), 395502, (19pp), xURL http://www.quantum-espresso.org.

Golub, G.H., Van Loan, C.F., 1996. Matrix Computations, third ed. Johns Hopkins University Press, Baltimore.

Hiki, Y., 1981. Higher order elastic constants of solids. Annu. Rev. Mater. Sci. 11 (1), 51–73.

Hohenberg, P., Kohn, W., 1964. Inhomogeneous electron gas. Phys. Rev. B 136, B864–B871.

Huang, M., Yan, H., Heinz, T.F., Hone, J., 2010. Probing strain-induced electronic structure change in graphene by Raman spectroscopy. Nano Lett. 10 (10), 4074–4079.

Hyer, M.W., 2009. Stress Analysis of Fiber-Reinforced Composite Materials. Destech Publications Inc, Lancaster.

Inamuddin, Boddula, R., Asiri, A.M., 2019. Black Phosphorus, first ed. Springer, Switzerland, Gewerbestrasse.

Jia, D., 2015. Mechanical and thermal properties of two-dimensional material. (Ph.D. thesis). University of North Carolina at Charlotte,

Jiang, J.-W., Park, H.S., 2014. Mechanical properties of single-layer black phosphorus. J. Phys. D Appl. 47 (38), 385304.

Kohn, W., Sham, L., 1965. Self-consistent equations including exchange and correlation effects. Phy. Rev. A 140, A1133–A1138.

Kokalj, A., 1999. XCrySDen—A new program for displaying crystalline structures and electron densities. J. Mol. Graph. Model. 17 (3), 176–179. http://dx.doi.org/10.1016/S1093-3263(99)00028-5.

Lawson, C.L., Hanson, R.J., 1974. Solving Least Squares Problems. Prentice Hall, Englewood.

Lee, J.G., 2017. Computational Materials Science: An Introductions, second ed. CRC Press, Boca Ranton.

Lee, K., Gatensby, R., McEvoy, N., Hallam, T., Duesberg, G.S., 2013. High-performance sensors based on molybdenum disulfide thin films. Adv. Mater. 25 (46), 6699–6702.

Lejaeghere, K., Bihlmayer, G., Bjorkman, T., Blaha, P., Blugel, S., Blum, V., Caliste, D., Castelli, I.E., Clark, S.J., Dal Corso, A., de Gironcoli, S., Deutsch, T., Dewhurst, J.K., Di Marco, I., xl, C., Dulak, M., Eriksson, O., Flores-Livas, J.A., Garrity, K.F., Genovese, L., Giannozzi, P., Giantomassi, M., Goedecker, S., Gonze, X., Granas, O., Gross, E.K.U., Gulans, A., Gygi, F., Hamann, D.R., Hasnip, P.J., Holzwarth, N.A.W., Iusan, D., Jochym, D.B., Jollet, F., Jones, D., Kresse, G., Koepernik, K., Kucukbenli, E., Kvashnin, Y.O., Locht, I.L.M., Lubeck, S., Marsman, M., Marzari, N., Nitzsche, U., Nordstrom, L., Ozaki, T., Paulatto, L., Pickard, C.J., Poelmans, W., Probert, M.I.J., Refson, K., Richter, M., Rignanese, G.M., Saha, S., Scheffler, M., Schlipf, M., Schwarz, K., Sharma, S., Tavazza, F., Thunstrom, P., Tkatchenko, A., Torrent, M., Vanderbilt, D., van Setten, M.J., Van Speybroeck, V., Wills, J.M., Yates, J.R., Zhang, G.X., Cottenier, S., Los Alamos National Lab. (LANL), Los Alamos, N.U.S., 2016. Reproducibility in density functional theory calculations of solids. Science (Amer. Assoc. Adv. Sci.) 351 (6280), 1415–U81.

Łepkowski, S., 2020. First-principles calculation of higher-order elastic constants using exact deformation-gradient tensors. Phys. Rev. B 102 (13), 134116.

Li, L., Yang, J., 2018. On mechanical behaviors of few-layer black phosphorus. Sci. Rep. 8 (1), 3227–8.

Ling, X., Wang, H., Huang, S., Xia, F., Dresselhaus, M.S., 2015. The renaissance of black phosphorus. Proc. Natl. A. Sci. USA 112 (15), 4523–4530.

Liu, N., Hong, J., Pidaparti, R., Wang, X., 2016. Fracture patterns and the energy release rate of phosphorene. Nanoscale 8 (10), 5728.

Liu, F., Ming, P., Li, J., 2007. Ab initio calculation of ideal strength and phonon instability of graphene under tension. Phys. Rev. B 76 (6).

Mehboudi, M., Dorio, A.M., Zhu, W., van der Zande, A., Churchill, H.O.H., Pacheco-Sanjuan, A.A., Harriss, E.O., Kumar, P., Barraza-Lopez, S., 2016. Two-dimensional disorder in black phosphorus and monochalcogenide monolayers. Nano Lett. 16 (3), 1704–1712.

Monkhorst, H.J., Pack, J.D., 1976. Special points for brillouin-zone integrations. Phys. Rev. B 13 (12), 5188–5192. http://dx.doi.org/10.1103/PhysRevB.13.5188.

Mukhopadhyay, T., Mahata, A., Adhikari, S., Zaeem, M.A., 2017. Effective mechanical properties of multilayer nano-heterostructures. Sci. Rep. 7 (1), 15818-15813.

Murnaghan, F.D., 1937. Finite deformations of an elastic solid. Am. J. Math. 59, 235–260.

Nye, J., 1985. Physical Properties of Crystals, second ed. Oxford Science Publications, New York.

Papageorgiou, D.G., Kinloch, I.A., Young, R.J., 2017. Mechanical properties of graphene and graphene-based nanocomposites. Prog. Mater. Sci. 90, 75–127.

Peng, Q., 2020. High-order nonlinear mechanical properties of g-SiC. Mech. Mater. 148, 103473.

Peng, Q., Ji, W., De, S., 2012a. Mechanical properties of graphyne monolayers: A first-principles study. Phys. Chem. Chem. Phys. 14 (38), 13385–13391.

Peng, Q., Ji, W., De, S., 2012b. Mechanical properties of the hexagonal boron nitride monolayer: Ab initio study. Comput. Mater. Sci. 56, 11–17.

Peng, Q., Liang, C., Ji, W., De, S., 2013. A first-principles study of the mechanical properties of g-GeC. Mech. Mater. 64, 135–141.

Perdew, J.P., Burke, K., Ernzerhof, M., 1996. Generalized gradient approximation made simple. Phys. Rev. Lett. 77 (18), 3865–3868.

Pinter, C.C., 1990. A Book of Asbtract Algebra, Dover Dover publications, Mineola, pp. 82–84.

Prandini, G., Marrazzo, A., Castelli, I.E., Mounet, N., Marzari, N., 2018. Precision and efficiency in solid-state pseudopotential calculations. Npj Comput. Mater. 4 (1), 1–13.

Setoodeh, A.R., Farahmand, H., 2018. Nonlinear modeling of crystal system transition of black phosphorus using continuum-DFT model. J. Phys. Condens. Matter 30 (3), 035901.

Slaughter, W.S., 2002. The Linearized Theory of Elasticity, first ed. Birkhäuser, Boston.

Strang, G., 1986. Introduction to Applied Mathematics, first ed. Wellesley-Cambridge Press, Wellesley.

Tadmor, E.B., Miller, R.E., 2016. Modelling Materials: Continuum, Atomistic and Multiscale Techniques, first ed. Cambridge University Press, Cambridge UK.

Tao, J., Shen, W., Wu, S., Liu, L., Feng, Z., Wang, C., Hu, C., Yao, P., Zhang, H., Pang, W., Duan, X., Liu, J., Zhou, C., Zhang, D., 2015. Mechanical and electrical anisotropy of few-layer black phosphorus. ACS Nano 9 (11), 11362–11370.

Towns, J., Cockerill, T., Dahan, M., Foster, I., Gaither, K., Grimshaw, A., Hazlewood, V., Lathrop, S., Lifka, D., Peterson, G.D., Roskies, R., Scott, J.R., Wilkins-Diehr, N., 2014. XSEDE: Accelerating scientific discovery. Comput. Sci. Eng. 16 (5), 62–74. http://dx.doi.org/10.1109/MCSE.2014.80, URL.

Voigt, W., 1910. Lehrbuch der Kristallphysik. B.G. Teubner, Berlin.

Wang, L., Kutana, A., Zou, X., Yakobson, B.I., 2015. Electro-mechanical anisotropy of phosphorene. Nanoscale 7 (21), 9746–9751.

Wei, X., Fragneaud, B., Marianetti, C.A., Kysar, J.W., 2009. Nonlinear elastic behavior of graphene: Ab initio calculations to continuum description. Phys. Rev. B 80, 250407.

Xiao, J.-K., Zhang, W., Liu, L.-M., Zhang, L., Zhang, C., 2016. Cracking of polycrystalline graphene on copper under tension. ACS Nano 384–385, 61–71.

Xu, M., Paci, J.T., Oswald, J., Belytschko, T., 2012. A constitutive equation for graphene based on density functional theory. Int. J. Solid Struct. 49, 2582–2589.

Yang, G., Huang, Z., Gao, C.-F., Zhang, B., 2016. Theoretical consideration of a microcontinuum model of graphene. AIP Adv. 6 (5), 55115–055115–10.

Zakharchenko, K.V., Katsnelson, M.I., Fasolino, A., 2009. Finite temperature lattice properties of graphene beyond the quasiharmonic approximation. Phys. Rev. Lett. 102 (4), 046808.